Journal of Rock Mechanics and Geotechnical Engineering 14 (2022) 505–526

Contents lists available at ScienceDirect

Journal of Rock Mechanics and Geotechnical Engineering

journal homepage: www.jrmge.cn

Full Length Article

Face stability of shield tunnels considering a kinematically admissible velocity field of soil arching

Wei Li [a,b], Chengping Zhang [a,b,*], Dingli Zhang [a,b], Zijian Ye [a,b], Zhibiao Tan [a,b]

[a] Key Laboratory for Urban Underground Engineering of the Ministry of Education, Beijing Jiaotong University, Beijing, 100044, China
[b] School of Civil Engineering, Beijing Jiaotong University, Beijing, 100044, China

ARTICLE INFO

Article history:
Received 7 January 2021
Received in revised form
4 June 2021
Accepted 18 October 2021
Available online 13 December 2021

Keywords:
Tunnel face stability
Velocity field
Failure pattern
Improved failure mechanism
Critical face pressure

ABSTRACT

Existing mechanism of simulating soil movement at tunnel face is generally based on the translational or rotational velocity field, which is, to some extent, different from the real soil movement in the arching zone. Numerical simulations are carried out first to investigate the characteristics of the velocity distribution at tunnel face and above tunnel vault. Then a new kinematically admissible velocity field is proposed to improve the description of the soil movement according to the results of the numerical simulation. Based on the proposed velocity field, an improved failure mechanism is constructed adopting the spatial discretization technique, which takes into account soil arching effect and plastic deformation within soil mass. Finally, the critical face pressure and the proposed mechanism are compared with the results of the numerical simulation, existing analytical studies and experimental tests to verify the accuracy and improvement of the presented method. The proposed mechanism can serve as an alternative approach for the face stability analysis.

© 2022 Institute of Rock and Soil Mechanics, Chinese Academy of Sciences. Production and hosting by Elsevier B.V. This is an open access article under the CC BY-NC-ND license (http://creativecommons.org/licenses/by-nc-nd/4.0/).

1. Introduction

Tunnel face stability problems have been receiving increasing attention. For engineering safety, it is crucial to control the face support pressure during the tunneling process for preventing tunnel face collapse and the subsidence of ground surface. To avoid face collapse and maintain face stability, the required minimal support pressure should be determined. It is thus desirable to establish a practical face failure mechanism and obtain a precise solution to the critical face pressure.

The stability of tunnel face has been investigated by many researchers. The existing approaches include the analytical method, experimental tests and numerical simulation. Both the numerical simulations (Augarde et al., 2003; De Buhan et al., 1999; Vermeer et al., 2002; Chen et al., 2011; Ukritchon and Keawsawasvong, 2017; Ukritchon et al., 2017a, b; Keawsawasvong and Ukritchon, 2019; Du et al., 2020; Shiau and Al-Asadi, 2020) and experimental tests (Broms and Bennermark, 1967; Mair, 1969; Schofield, 1980; Atkinson and Potts, 1977; Chambon and Corte, 1994; Takano et al., 2006; Kirsch, 2010; Idinger et al., 2011; Chen et al., 2013) have been extensively performed to visualize the failure pattern of a tunnel face. The advantage of the numerical simulation lies in its good repeatability (Huang et al., 2018a; Ukritchon and Keawsawasvong, 2019a, b, c), while the experimental tests are good at capturing the characteristic of the face failure. As shown in Fig. 1, when the tunnel face collapses, a soil arching and a shear band are formed above the tunnel face and ahead of the tunnel face, respectively, which could be adequately simulated with logarithmic spirals.

The limit analysis and limit equilibrium are two effective analytical methods to examine the face stability. The limit equilibrium method usually assumes the calculation model to deduce critical face pressures and consider different influence factors (Anagnostou and Kovári, 1996; Anagnostou, 2012; Anagnostou and Perazzelli, 2013, 2015; Perazzelli et al., 2014). The limit analysis consists of the upper and lower bound theorems, which result in the upper and lower bound solutions of critical loads by constructing kinematic and static mechanisms, respectively. A simple and intuitive kinematic mechanism was the rigid block failure mechanism based on the translational velocity field, which was first introduced by Davis et al. (1980) and Leca and Dormieux (1990), as shown in Fig. 2a. Then, the failure mechanisms of the

* Corresponding author. Key Laboratory for Urban Underground Engineering of the Ministry of Education, Beijing Jiaotong University, Beijing, 100044, China.
E-mail address: chpzhang@bjtu.edu.cn (C. Zhang).

Peer review under responsibility of Institute of Rock and Soil Mechanics, Chinese Academy of Sciences.

https://doi.org/10.1016/j.jrmge.2021.10.006
1674-7755 © 2022 Institute of Rock and Soil Mechanics, Chinese Academy of Sciences. Production and hosting by Elsevier B.V. This is an open access article under the CC BY-NC-ND license (http://creativecommons.org/licenses/by-nc-nd/4.0/).

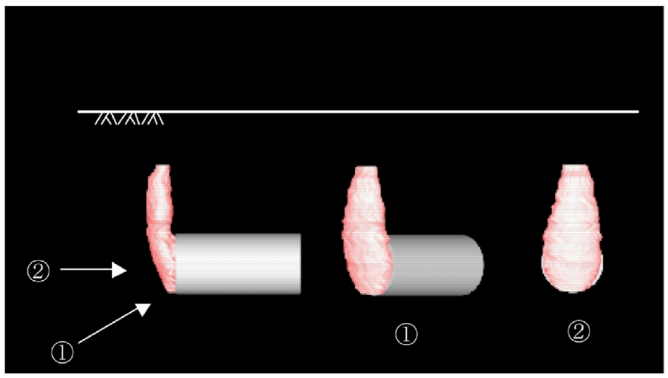

Fig. 1. Three-dimensional (3D) failure zone (Takano et al., 2006).

translational multi-block (Mollon et al., 2009) and the rotational rigid block (Subrin and Wong, 2002) were proposed to improve the velocity field and allow freer development of the shear failure plane, as shown in Fig. 2b and c. However, the failure mechanisms mentioned above suffered from the fact that only a portion of the tunnel face collapses but the remaining region was undisturbed. To overcome this shortcoming, an innovative spatial discretization technique was proposed by Mollon et al. (2010, 2011) to enhance the knowledge about the failure mechanism. Based on these failure mechanisms, researches on face stability influence factors and improvement methods were widely conducted (Zhang et al., 2015; Han et al., 2016a, b; Pan and Dias, 2016a, b, 2017; Zou and Qian, 2018; Ding et al., 2018, 2019; Li et al., 2018, 2019a, b; Zou et al., 2019a, b; Li and Zhang, 2020). Moreover, a continuous velocity field was proposed by Mollon et al. (2013) for purely cohesive soils, which significantly improved the existing upper solutions. The proposed velocity field closely simulates the movement of the purely cohesive soils and provided better results for the related geotechnical problems (Osman et al., 2006; Klar et al., 2007; Klar and Klein, 2014; Huang et al., 2018b; Zhang et al., 2018a, b; Li et al., 2019c; Zhang et al., 2020).

It can be found from the extensive literature review that the accuracy of the upper bound solution is closely related to the adopted kinematically admissible mechanism. The accuracy of the obtained critical face pressure and the correspondence of the failure mechanism to the real situation can be improved with increasing sensibility and credibility of the velocity field. However, most reported studies neglected or simplified the soil movement in the arching zone. Fig. 2 shows that the simplified translational or rotational rigid movement used in the analytical method leads to a cone or 'horn' shape of the failure mechanism. Therefore, this paper intends to mitigate this problem by proposing a new kinematically admissible velocity field for the soil archinging zone.

Inspired by the advantages of a more promising and reasonable kinematically admissible velocity field, this paper aims at exploring a more realistic velocity field for the tunnel face in frictional soils. Numerical simulations will be carried out first to investigate the characteristics of the velocity distribution at the tunnel face and above the tunnel vault. Then, a kinematically admissible velocity field will be defined and deduced in detail to better correspond to the real soil movement. Finally, comparisons among the presented study, the numerical simulation and other existing studies will be performed to verify the accuracy and improvement of the proposed mechanism.

2. Numerical simulations

2.1. Numerical model

To investigate the face stability of shield tunnels, FLAC3D is adopted to perform the numerical simulation. The failure or unstable state of the system is determined by the unbalanced force ratio, which is defined as the ratio of the average unbalanced mechanical force to the average applied mechanical force for all the grid points at each calculation step. This unbalanced force ratio will decrease with the calculation step. A steady stable state will be achieved when the unbalanced force ratio is under a prescribed tolerance value (10^{-5} is usually set as the default value). But when the unbalanced force ratio tends to attain a quasi-constant value that is larger than the prescribed tolerance value, it means that an unstable state or a steady plastic flow of the system is reached. In this case, the infinitely increasing displacements and failure of the numerical model will occur.

A 3D numerical model with the diameter to depth ratios C/D varying from 0.5 to 3 is built. Fig. 3 presents a half model of a shield tunnel with a diameter of $D = 10$ m and $C/D = 2$. The model contains 90,675 zones and the dimensions are $3D \times 4D \times (2D + C)$ in the X, Y and Z directions to counteract the boundary effect. As for the boundary conditions, the top of the model (representing ground surface) is set free, the four sides are constrained horizontally and the bottom face is fixed.

Four types of soils are adopted and shown in Table 1. Soils are assigned with the Mohr-Coulomb failure criterion, which corresponds to a shear failure condition of a frictional soil. The Young's

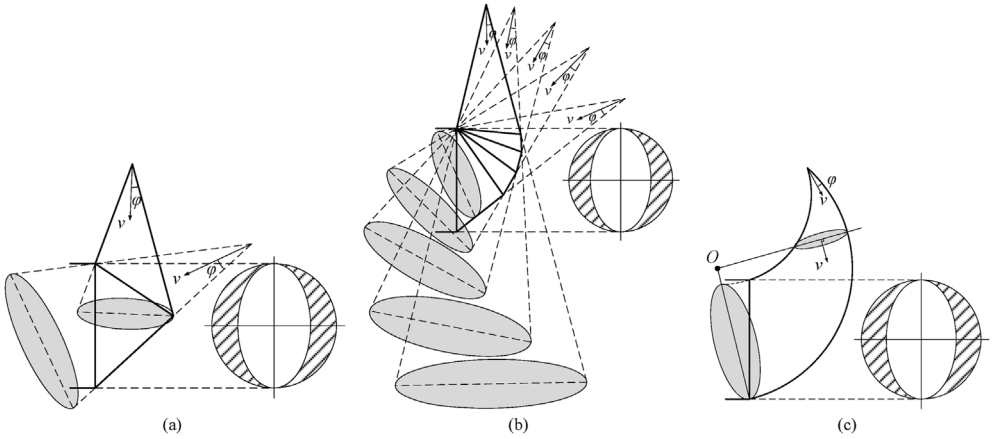

Fig. 2. Existing failure mechanisms: (a) Two-block, (b) Multi-block, and (c) 'Horn' shape. v and φ represent the velocity vector and internal friction angle, respectively.

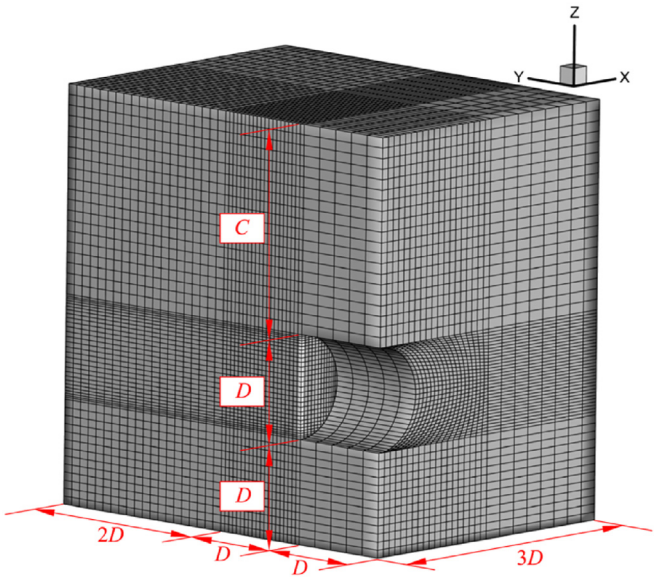

Fig. 3. Numerical model of a circular shield tunnel.

modulus $E = 20$ MPa is used (Mollon et al., 2013; Ukritchon et al., 2017b; Huang et al., 2018b). The empirical equation $K = 1 - \sin\varphi$ for the earth pressure coefficient at rest is adopted to calculate the value of K, where φ is the internal friction angle of the soil. The value of the Poisson's ratio ν is determined according to the relation $\nu = K/(1 + K)$ between the earth pressure coefficient and the Poisson's ratio. Moreover, the shell structural element with a thickness of 0.35 m is adopted to model the tunnel lining, which is assigned with the Young's modulus $E = 35$ GPa and the Poisson's ratio $\nu = 0.25$. During the simulation process, a length of 10 m of the tunnel is excavated. After the excavation, the zone behind tunnel face is installed with lining, simulated by shell elements, instantly.

Without a priori assumption on the critical state of the tunnel face, the determination of the critical collapse pressure is proceeded by the stress-controlled method. First, the tunnel face is applied with a uniformly distributed face pressure to maintain its force balance. Second, the displacement of tunnel face is monitored with the decrease of the support pressure in each calculation cycle. Finally, when the tunnel face collapses or the plastic flow occurs after a tiny decrement of the support pressure, the face pressure at this moment is noted and considered as the critical face pressure.

2.2. Results of the numerical simulations

2.2.1. Critical face pressure

Fig. 4 shows the face pressure ratio n versus the horizontal displacement of tunnel face with different relative buried depth ratios C/D and different types of soils. The face pressure ratio is defined as follows:

$$\sigma_t^{\text{applied}} = nK\gamma(C + D/2) \quad (1)$$

where n defines the ratio of the face pressure to the horizontal earth stress, $\sigma_t^{\text{applied}}$ is the face pressure, and γ is the unit weight of soils.

It is shown that the horizontal face displacement increases rapidly with the decrease of the face pressure ratio. The critical value of n is determined when the slope of the curve approximates 0. The dotted lines in Fig. 4 represent the critical value of n. It is found that a higher critical support pressure ratio is obtained for a smaller C/D. Besides, differences between Fig. 4a and b shows that a smaller critical face pressure ratio is needed for soils with a higher shear strength. It is correspondingly expected that when the shear strength of soils is higher, a smaller face pressure is required.

Table 1
Soil conditions of the tunnel face.

C/D	γ (kN/m^3)	K	ν	c (kPa)	φ (°)	Soil type
0.5, 1, 1.5, 2, 2.5, 3	18	0.658	0.397	0	20	Loose sands
		0.357	0.263	0	40	Dense sands
		0.708	0.414	7	17	Soft clays
		0.577	0.366	10	26	Stiff clays

Note: c represents the cohesion of the soil.

2.2.2. Velocity distribution at the tunnel face

As aforementioned, the translational and rotational velocity fields are two commonly used mechanisms for tunnel face problem. In order to make further investigation on failure mechanism of tunnel face, this section will perform several numerical simulations to study the velocity distribution at the tunnel face. The velocity field of the numerical simulations will be compared with the translational and rotational velocity fields usually adopted in the existing analytical approaches. The obtained velocity inclination at the tunnel face is defined in Fig. 5. The velocity vectors of monitoring points distributed on the whole tunnel face are collected and recorded in the numerical simulation. The velocity inclination α represents the angle between the velocity vector of the monitoring point and the opposite excavation direction (negative Y-coordinate), which can be calculated by the equation $\alpha = \arccos[-v_y/(v_x^2+v_y^2+v_z^2)^{0.5}]$.

The velocity inclinations at the tunnel face in clays and sands for different depth to diameter ratios C/D are provided in Figs. 6 and 7. The velocity inclinations at the tunnel face are similar in clays and sands, both increase with the Z-coordinate. The rotational velocity field is basically consistent with the velocity inclination obtained from the numerical simulations. It is shown that the rotational velocity field well estimates the velocity distribution at the tunnel face. But the velocity inclination of the translational velocity field keeps constant with the Z-coordinate, which oversimplifies the soil movement at the tunnel face. Besides, it is found that the points of the numerical simulations on both ends of curves and the points far away from the vertical symmetric plane of the tunnel face ($X \geq 0.4D$) deviate from the curves estimated by the rotational velocity field. This is because the velocity direction near the tunnel face edge will be inevitably affected by the face boundary in the numerical simulation, but the rotational velocity field assumes that the soils at the tunnel face move together as a rigid block. It is considered that the rotational velocity field still accurately simulates the soil movement of most parts of the tunnel face and the rotational velocity field is sufficiently reliable to represent the velocity at the tunnel face.

2.2.3. Velocity distribution at the tunnel vault

This section will present the velocity distribution at the tunnel vault obtained from the numerical simulation. The comparisons of the velocity inclination provided by the numerical simulations, the translational and rotational velocity fields are performed. The velocity inclination at the tunnel vault is defined in Fig. 8. As shown in Fig. 8, the velocity vectors of the monitoring points distributed on the whole horizontal plane Z_1 are collected and recorded in the numerical simulation. The plane Z_1 has a length of D and a width of D, which is located at the tunnel vault. Similarly, the velocity inclination of the monitoring point of the tunnel vault is also

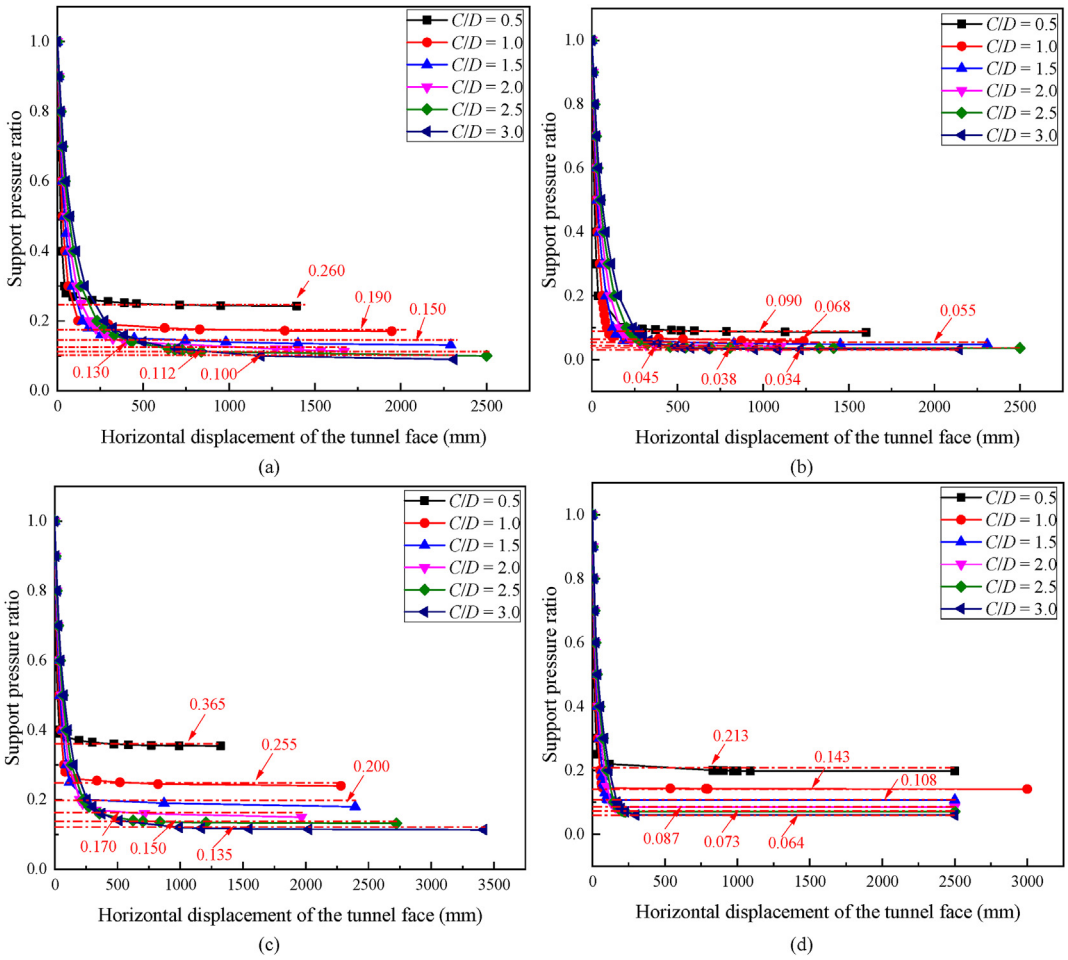

Fig. 4. Curves of the face pressure ratio versus the horizontal displacement of tunnel face: (a) $c = 7$ kPa and $\varphi = 17°$, (b) $c = 10$ kPa and $\varphi = 25°$, (c) $c = 0$ kPa and $\varphi = 20°$, and (d) $c = 0$ kPa and $\varphi = 40°$.

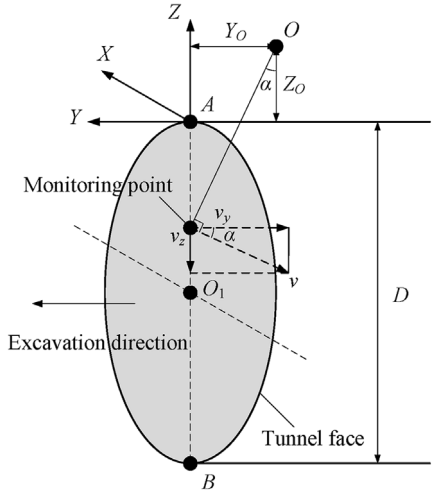

Fig. 5. Schematic diagram of the velocity inclination at the tunnel face in the numerical simulation.

defined as the angle between the velocity vector and the opposite excavation direction.

Figs. 9 and 10 show the velocity inclination at the tunnel vault obtained from the numerical simulations for clays and sands. It is shown that the velocity inclinations at the tunnel vault in the numerical simulation generally decrease with the *Y*-coordinate, which is almost the same in both clays and sands. However, the velocity inclination estimated by the rotational velocity field increases with the *Y*-coordinate, which is totally different from the results of the numerical simulation. This difference reveals that the rotational velocity field fails to represent the soil movement with arching effect. The constant velocity inclination of the translational velocity field also falls short of representing the variation characteristic of the velocity at the tunnel vault. Besides, it is shown that the velocity inclinations of the grid points far away from the vertical symmetric plane ($X > 0.5D$) have a different variation trend compared with those of the other points. This situation is caused by the soil arching effect. When $X/D > 0.5$, the grid points are beyond the soil arching and located at the region of the undisturbed soils, and thus the velocity inclinations of these undisturbed points are different from others.

2.3. Comparisons between the numerical simulations and the experimental tests

To verify the obtained numerical results, the failure patterns of three typical experimental tests (Chambon and Corte, 1994; Kirsch, 2010; Idinger et al., 2011) are adopted to compare with the failure zone obtained from FLAC3D. It is shown in Fig. 11 that the failure patterns of the experimental tests are basically

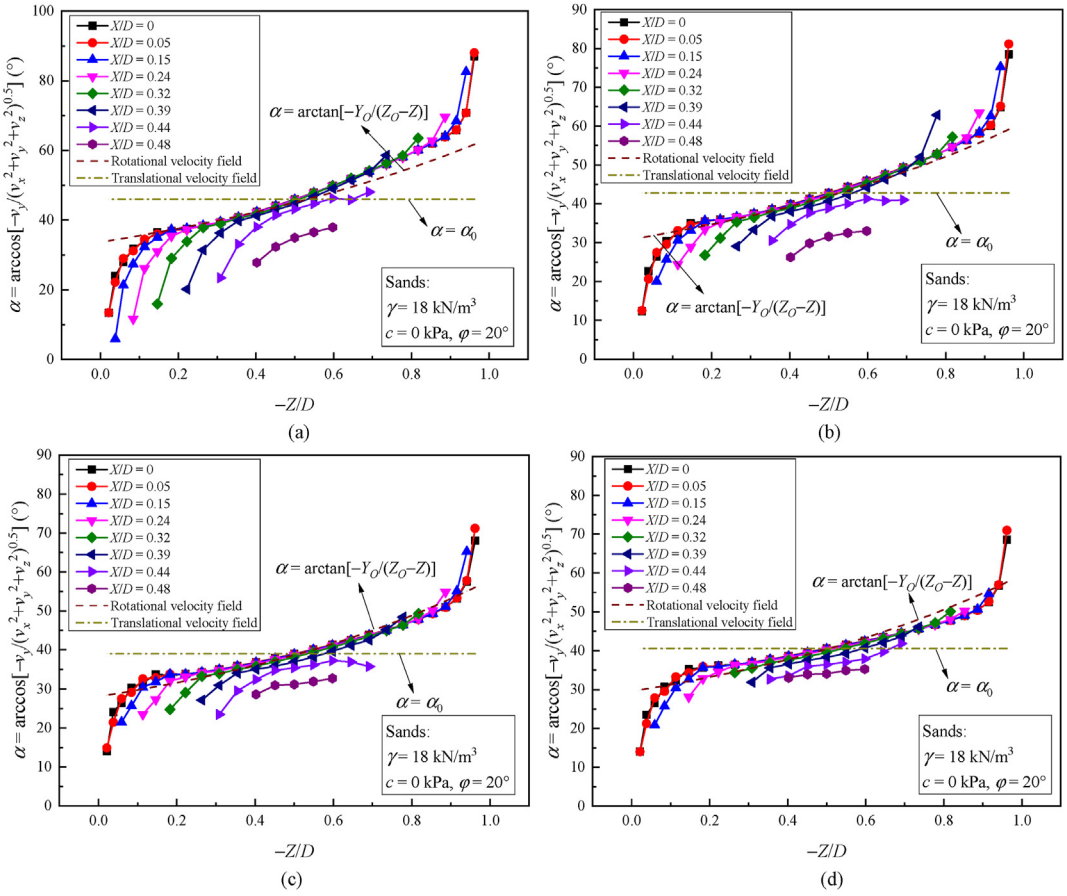

Fig. 6. Velocity inclination at the tunnel face in sands: (a) $C/D = 0.5$, (b) $C/D = 1$, (c) $C/D = 2$, and (d) $C/D = 3$.

consistent with that of the numerical simulation, especially for the shear failure band obtained from the experimental test by Idinger et al. (2011). Compared with the failure patterns obtained from the experimental tests, the numerical simulation provides a more conservative estimate of the failure range of the tunnel face. Thus, although the finite difference code FLAC cannot predict the soil behavior perfectly, the numerical simulation of FLAC3D is still a reliable tool to study the stability problem of tunnel faces.

Furthermore, Table 2 presents the comparisons of the normalized critical face pressure provided by the numerical simulation in this paper and other experimental tests. The numerical method and experimental test are inherently different in the determination of the critical state of the tunnel face failure. But it is shown that the normalized critical face pressures obtained from this study approximate the existing experimental results. Only some numerical results are slightly of larger values than the experimental results. This comparison also implies that the numerical simulation can be used to investigate the tunnel face stability problem and the numerical results are relatively effective and reasonable.

3. Construction of the improved failure mechanism

As mentioned above, the rotational and translational velocity fields are two commonly used kinematically admissible velocity fields for the face stability analysis in frictional soils. Compared with the translational velocity field, the rotational velocity field can simulate the soil movement at the tunnel face well. However, for the region above the tunnel vault, both the rotational and translational velocity fields are different from that of the numerical simulation, which fail to reflect the characteristic of the velocity distribution. Thus, this section aims at describing a new kinematically admissible velocity field for the soil arching zone based on the results of the numerical simulations to improve the representation of the soil movement with arching effect. An improved failure mechanism is newly constructed based on this proposed velocity field using the spatial discretization technique. In the proposed failure mechanism, a perfectly plastic soil material is assumed. The Mohr-Coulomb failure criterion and the associated flow rule are adopted. Finally, based on the upper bound method of the limit analysis theorem, the critical face pressure is derived by equating the rate of external work to the rate of energy dissipation.

This paper adopts two different methods to construct the upper and lower failure mechanisms, respectively. The whole failure mechanism includes two parts, as shown in Fig. 12. Zone I represents the area ahead of the tunnel face (lower part) and the Zone II represents the region above the tunnel vault (upper part). Both zones are constructed by the spatial discretization technique. The lower part of the failure mechanism is constructed based on the rotational velocity field, while the upper part adopts a new kinematically admissible velocity field to generate the 3D failure surface.

3.1. Generation of the failure mechanism in Zone I

3.1.1. Principle of the point generation in Section 1 of Zone I

As shown in Fig. 13, there are $2n$ discretized points on the circular tunnel face in Section 1, denoted by A_j and A'_j $(1 \le j \le n)$. The

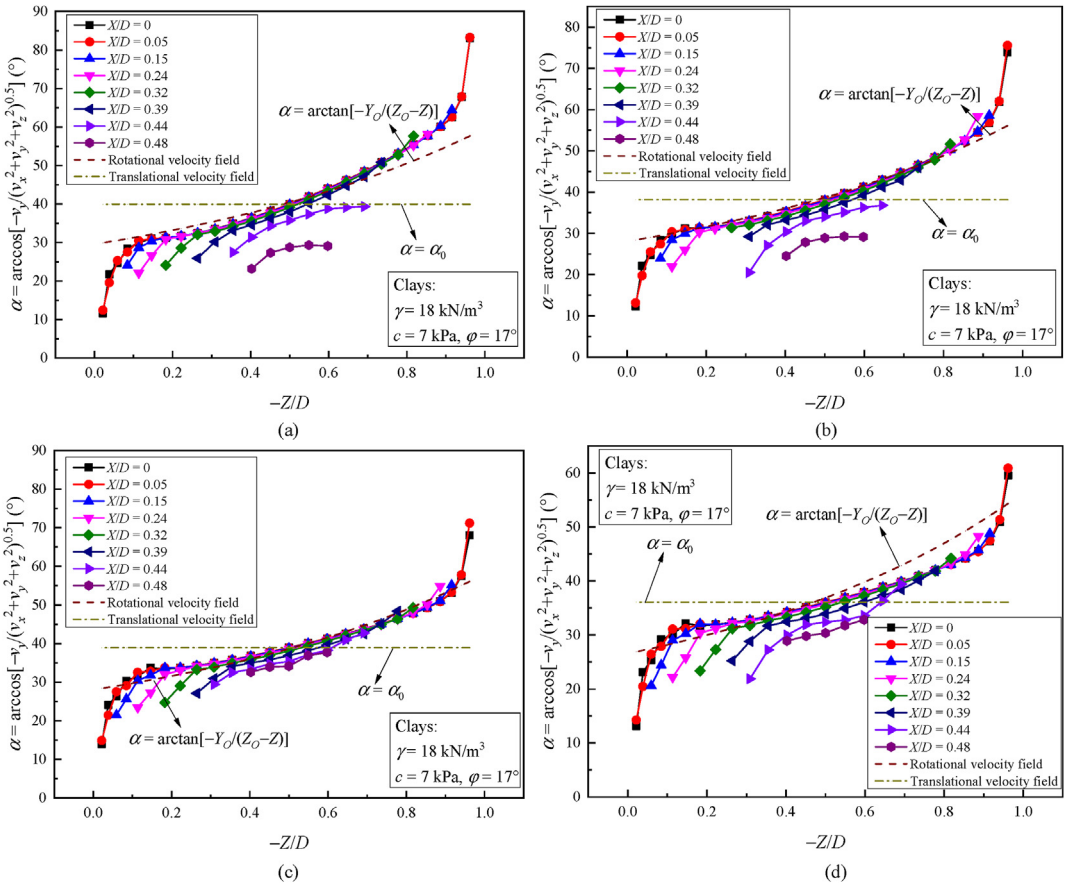

Fig. 7. Velocity inclination at the tunnel face in clays: (a) $C/D = 0.5$, (b) $C/D = 1$, (c) $C/D = 2$, and (d) $C/D = 3$.

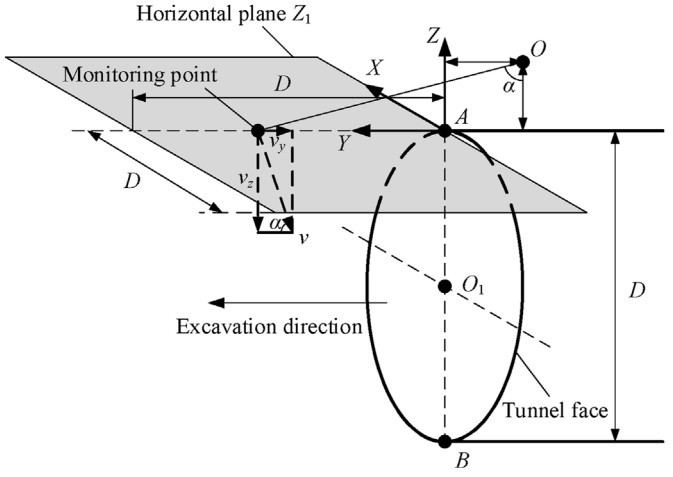

Fig. 8. Schematic diagram of the velocity inclination at the tunnel vault in the numerical simulation.

rotation center O of the rotational velocity field is located in the vertical symmetric plane. Each radial plane passing through the point O is named as Π_j, where $1 \le j \le n$. A_1 and A'_1 are the two first points to generate the mechanism of Section 1. These two points and point O constitute the radial plane Π_1, and the points A_1 and A'_1 are renamed as $P_{i,1}$ and $P_{i+1,1}$, respectively. A new point $P_{i,2}$ in the radial plane Π_2 is generated from the points $P_{i,1}$ and $P_{i+1,1}$ of Π_1. More generally, a new point $P_{i,j+1}$ in the radial plane Π_{j+1} is generated from the points $P_{i,j}$ and $P_{i+1,j}$ of Π_j, as shown in Fig. 14. The facet $F_{i,j}$ consists of the points $P_{i,j+1}$, $P_{i,j}$ and $P_{i+1,j}$, and all the triangular facets constitute the 3D failure surface. The point generation process should obey the normality condition and the quasi-uniformly distribution. The normality condition means that the angle between the outside normal vector $\vec{N}_{i,j}$ and the velocity vector is $\pi/2 + \varphi$. The quasi-uniformly distribution requires that all the new generated points $P_{i,j+1}$ are uniformly distributed in the plane Π_{j+1}, i.e. $\theta_{i,j+1} = (\theta_{i,j} + \theta_{i+1,j})/2$, where $P_{i,j+1} = (C_{j+1}, r_{i,j+1}, \theta_{i,j+1})$. In Section 1, there are $j-1$ new generated points and two existing points. This process of point generation continues until the last plane Π_n of Section 1.

3.1.2. *Principle of the point generation in Section 2 of Zone I*

After finishing the point generation in Section 1 of Zone I, a total of $n + 1$ points will be generated in the last radial plane Π_n. These $n + 1$ points will generate $n + 1$ new points in the radial plane Π_{n+1} of Section 2 of Zone I. Following the same normality condition and the quasi-uniformly distribution, the point generation will be successively conducted until the final point F, which represents the closure of the failure mechanism.

The spatial discretization technique is to overcome the shortcoming that only a portion of the circular tunnel face collapses, while the remaining area is at rest. Thus the 3D failure surface generated by the spatial discretization technique could not be described by a simple geometrical shape but a discretized surface. The accuracy of the discretized failure mechanism will highly depend on the fineness of the discretization parameters. More details on the mathematical formulation for the point generation of

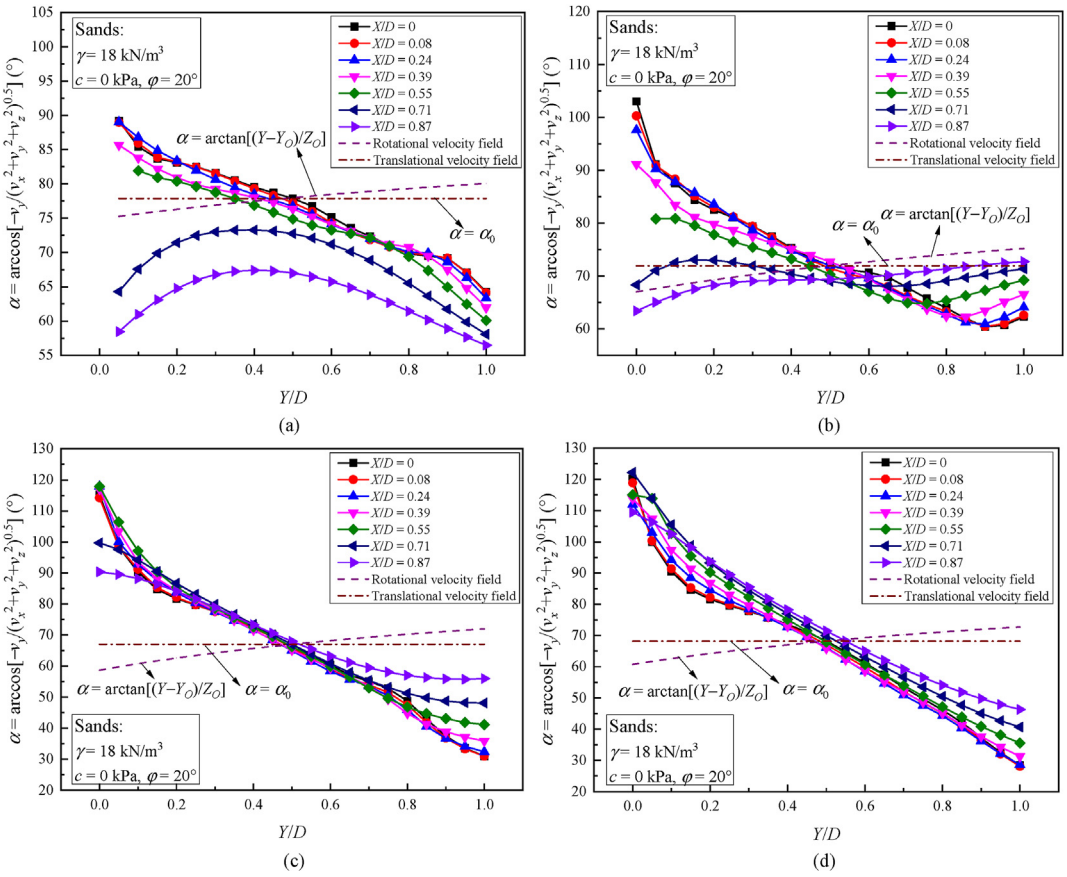

Fig. 9. Velocity inclination at the tunnel vault in sands: (a) $C/D = 0.5$, (b) $C/D = 1$, (c) $C/D = 2$, and (d) $C/D = 3$.

Sections 1 and 2 of Zone I can be referred to in Mollon et al. (2010, 2011).

3.2. Generation of the failure mechanism in Zone II

The generation of the 3D failure surface of Zone II begins with the intersection plane between Zones I and II. This section will propose a new kinematically admissible velocity field for the soil arching zone. The spatial discretization technique will also be adopted to generate the failure mechanism based on the proposed velocity field.

3.2.1. Proposed velocity field for Zone II

This section will present the new proposed velocity field above the tunnel vault. Zone II is divided into infinite vertical rigid blocks, each two adjacent rigid blocks are separated by a vertical *X*-*Z* plane. The velocity field of every rigid block is assumed as shown in Fig. 15. The velocity is assumed to be independent of both the *X*- and *Z*-coordinates but vary with the *Y*-coordinate. The formula of the velocity in Zone II is defined as follows:

$$v_{\mathrm{U}}(y) = v_{\mathrm{Uc}}\frac{\sin\varphi}{\sin[\varphi+\theta_{\mathrm{v}}(y)]} \tag{2}$$

where $v_{\mathrm{U}}(y)$ represents the velocity of Zones II; v_{Uc} is the velocity at the point C_{s1}, which is assumed to be vertically downward; and $\theta_{\mathrm{v}}(y)$ is the angle between the velocity vector and the negative direction of the *Z*-coordinate. In addition, when $\theta_{\mathrm{v}}(y)$ rotates counterclockwise, $\theta_{\mathrm{v}}(y)$ is defined as positive, otherwise negative. The verification of normality condition satisfaction of the proposed velocity field is provided in Appendix A.

According to the assumption on v_{Uc}, the condition of $\theta_{\mathrm{v}}(y)$ at the point C_{s1} can be obtained:

$$\theta_{\mathrm{v}}(y_{\mathrm{c}}) = 0 \tag{3}$$

where y_{c} is the *Y*-coordinate of the point C_{s1}.

As shown in Fig. 16, the velocity field should not only obey the normality condition in Zone II, but also be kinematically compatible with the rotational velocity field in Zone I. Thus the following conditions are required:

$$\left.\begin{aligned} v_{\mathrm{L}}(y) &= \omega\sqrt{z_O^2+(y-y_O)^2} \\ \alpha(y) &= \arccos\left[(y-y_O)\Big/\sqrt{(y-y_O)^2+z_O^2}\right] \\ \frac{v_{\mathrm{U}}(y)}{\sin[\alpha(y)-\varphi]} &= \frac{v_{\mathrm{L}}(y)}{\cos[\varphi-\theta_{\mathrm{v}}(y)]} = \frac{v_{\mathrm{LU}}(y)}{\cos[\alpha(y)-\theta_{\mathrm{v}}(y)]} \end{aligned}\right\} \tag{4}$$

where $v_{\mathrm{L}}(y)$ is the velocity in Zone I along the intersection plane of Zones I and II; ω represents the angular velocity in Zone I; $v_{\mathrm{LU}}(y)$ is the relative velocity between $v_{\mathrm{L}}(y)$ in Zone I and $v_{\mathrm{U}}(y)$ in Zone II; y_O and z_O are the coordinates of the rotational center in the vertical symmetric plane; and $\alpha(y)$ is the angle between the velocity vector $\boldsymbol{v}_{\mathrm{L}}(y)$ and the direction of *Y*-coordinate.

Combining Eqs. (2)–(4) can yield two relations between the rotational velocity field of Zone I and the proposed velocity field of Zone II. The first relation of $v_{\mathrm{U}}(y)$ is built based on any point in the intersection plane of Zones I and II. Any point in the intersection

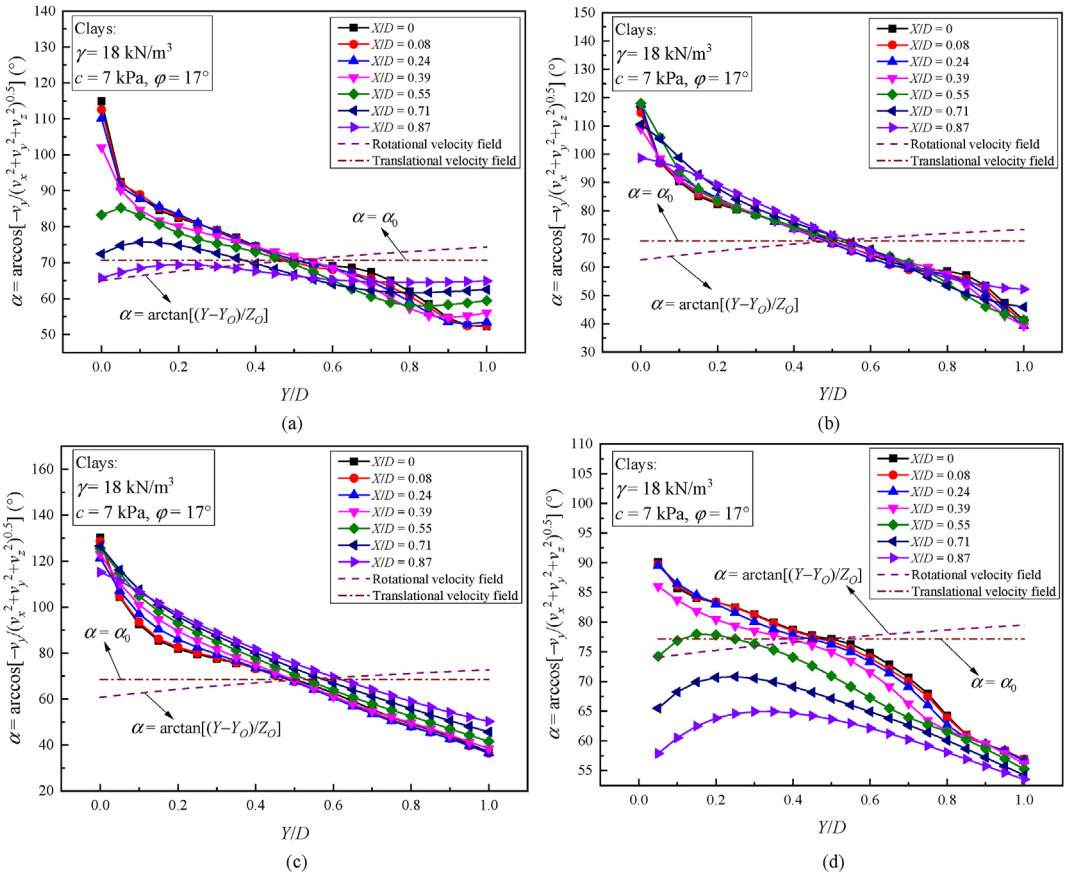

Fig. 10. Velocity inclination at the tunnel vault in clays: (a) $C/D = 0.5$, (b) $C/D = 1$, (c) $C/D = 2$, and (d) $C/D = 3$.

plane of Zones I and II must follow the triangular relationship as shown in Fig. 16. Particularly, when $y = y_c$, the second relation in Eq. (5) can be established.

$$v_U(y) = \begin{cases} \dfrac{v_L(y)}{\cos[\varphi - \theta_v(y)]} \sin[\alpha(y) - \varphi] \\ \dfrac{v_{Lc}}{\cos\varphi} \sin(\alpha_c - \varphi) \dfrac{\sin\varphi}{\sin[\varphi + \theta_v(y)]} \end{cases} \tag{5}$$

where v_{Lc} is the velocity of Zone II at the point C_{s1}, and α_c is the corresponding angle between the direction of Y-coordinate and the velocity $v_L(y)$ at the point C_{s1}. The formulae of v_{Lc} and α_c are expressed as follows:

$$\left.\begin{aligned} v_{Lc} &= v_L(y_c) = \omega\sqrt{z_0^2 + (y_c - y_O)^2} \\ \alpha_c &= \arccos\left[(y_c - y_O) \Big/ \sqrt{(y_c - y_O)^2 + z_0^2}\right] \end{aligned}\right\} \tag{6}$$

According to Eq. (5), the expression of $\theta_v(y)$ can be given by

$$\theta_v(y) = \arctan\left[\frac{F(y) - \tan\varphi}{1 - \tan\varphi F(y)}\right] \tag{7a}$$

where

$$\left.\begin{aligned} F(y) &= \frac{v_{Lc}}{v_L(y)} \frac{\sin(\alpha_c - \varphi)}{\sin[\alpha(y) - \varphi]} \tan\varphi = \frac{A}{y + B} \\ A &= (y_c - y_O - z_O \tan\varphi)\tan\varphi \\ B &= -y_O - z_O \tan\varphi \end{aligned}\right\} \tag{7b}$$

By substituting Eqs. (5)–(7) into Eq. (2), and with some simplification, the expression of v_{Uc} is represented as follows:

$$v_{Uc} = \omega(y_c - y_O - z_O \tan\varphi) \tag{8}$$

Thus Eq. (2) can be rewritten as follows:

$$v_U(y) = \omega(y_c - y_O - z_O \tan\varphi) \frac{\sin\varphi}{\sin[\varphi + \theta_v(y)]} \tag{9}$$

Eqs. (2)–(9) above can ensure that the normality condition is considered in both Zones I and II.

As shown in Fig. 17, the cross-section of the failure mechanism in Zone II is bounded by two curves emerging from points A and C, respectively (the tunnel vault and the right end of the intersection plane between Zones I and II). The two curves are defined as $z = f_1(y)$ and $z = f_2(y)$, respectively, and they will intersect at the final point C_{snh}. According to the normality condition, the following geometric conditions of the failure surface can be easily obtained:

$$\left.\begin{aligned} f_1'(y) &= \tan\left[\frac{\pi}{2} - \varphi + \theta_v(y)\right] \\ f_2'(y) &= \tan\left[\frac{\pi}{2} + \varphi + \theta_v(y)\right] \end{aligned}\right\} \tag{10}$$

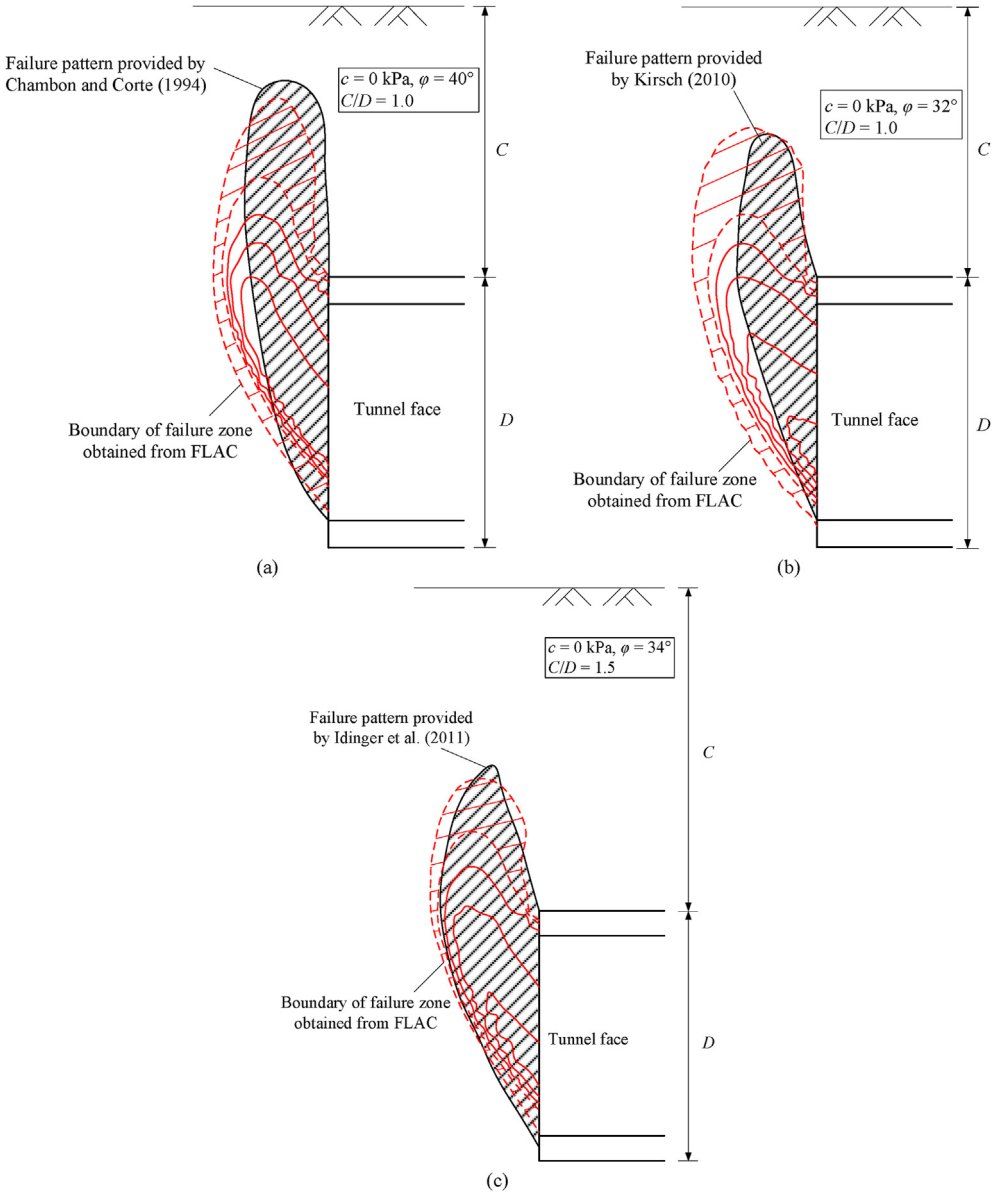

Fig. 11. Comparisons of the failure pattern between the numerical simulation and the experimental tests: (a) Comparison with the test by Chambon and Corte (1994), (b) Comparison with the test by Kirsch (2010), and (c) Comparison with the test by Idinger et al. (2011).

where $f_1'(y)$ and $f_2'(y)$ represent the angle between the direction of Y-coordinate and the velocity discontinuity surface.

By the integration of Eq. (10), the two curves of $z = f_1(y)$ and $z = f_2(y)$ can be obtained as follows:

where C_1 and C_2 are two integration constants, which can be obtained by substituting two boundary conditions into Eq. (11). The boundary conditions are as follows:

$$z = \begin{cases} f_1(y) = \dfrac{1-\tan^2\varphi}{2\tan\varphi}\left\{y + \dfrac{A\left(1+\tan^2\varphi\right)}{2\tan\varphi}\ln\left[\dfrac{2\tan\varphi}{1-\tan^2\varphi}(y+B) - \dfrac{A\left(1+\tan^2\varphi\right)}{1-\tan^2\varphi}\right]\right\} + C_1 \\ f_2(y) = -\dfrac{1+\tan^2\varphi}{2A\left(1-\tan^2\varphi\right)}y^2 + \left[\dfrac{2\tan\varphi}{1-\tan^2\varphi} - \dfrac{B\left(1+\tan^2\varphi\right)}{A\left(1-\tan^2\varphi\right)}\right]y + C_2 \end{cases} \tag{11}$$

Table 2
Comparisons of the normalized critical face pressure.

Source	Soil conditions and tunnel geometry	Normalized critical face pressure, $\sigma_t/(\gamma D)$	Numerical results ($\sigma_t/(\gamma D)$) obtained from this study
Chambon and Corte (1994)	$c = 0$ kPa, $\varphi = 38°–42°$, $D = 10$ m, $C/D = 1$ and 2	0.046 for $C/D = 1$ 0.05 for $C/D = 2$	0.052 for $C/D = 1$ 0.057 for $C/D = 2$
Chen et al. (2013)	$c = 0$ kPa, $\varphi = 37°$, $D = 1$ m, $C/D = 0.5$, 1 and 2	0.065 for $C/D = 0.5$ 0.076 for $C/D = 1$ 0.072 for $C/D = 2$	0.07 for $C/D = 0.5$ 0.078 for $C/D = 1$ 0.08 for $C/D = 2$
Kirsch (2010)	$c = 0$ kPa, $\varphi = 30°–34°$, $D = 0.1$ m, $C/D = 0.5$, 1 and 1.5	0.07–0.18 for $C/D = 0.5$ 0.08–0.15 for $C/D = 1$ 0.09–0.16 for $C/D = 1.5$	0.109 for $C/D = 0.5$ 0.114 for $C/D = 1$ 0.113 for $C/D = 1.5$
Idinger et al. (2011)	$c = 0$ kPa, $\varphi = 34°$, $D = 2.5$ m, 5 m and 7.5 m, $C/D = 0.5$, 1 and 1.5	0.08 for $C/D = 0.5$ 0.08 for $C/D = 1$ 0.12 for $C/D = 1.5$	0.088 for $C/D = 0.5$ 0.103 for $C/D = 1$ 0.097 for $C/D = 1.5$

Note: Some experimental results varied in the same tests.

$$\left.\begin{aligned} f_1(y_A) &= 0 \\ f_2(y_C) &= 0 \end{aligned}\right\} \tag{12}$$

where y_A and y_C represent the Y-coordinates of the points A and C, respectively.

By equating $f_1(y)$ to $f_2(y)$, the coordinates of the point C_{snh} are obtained:

$$\left.\begin{aligned} x_{C_s} &= 0 \\ f_1(y_{C_s}) &= f_2(y_{C_s}) \Rightarrow y_{C_s} = y_c \\ z_{C_s} &= f_1(y_{C_s}) = f_2(y_{C_s}) \end{aligned}\right\} \tag{13}$$

where $(0, y_{Cs}, z_{Cs})$ are the coordinates of the point C_{snh}. Similarly, the coordinates of the point C_{s1} are $(0, y_{Cs}, 0)$. Zone II is uniformly divided into n_h parts in the vertical direction by several horizontal planes, in which $n_h = (z_{Cs}/\delta_H)$ and δ_H is the distance between each two adjacent horizontal planes.

Both the velocity fields in Zones I and II are defined by the coordinates of the point O (y_O and z_O). The shape of the proposed failure mechanism varies with y_O and z_O, and the critical failure pattern can be obtained by the optimization of y_O and z_O.

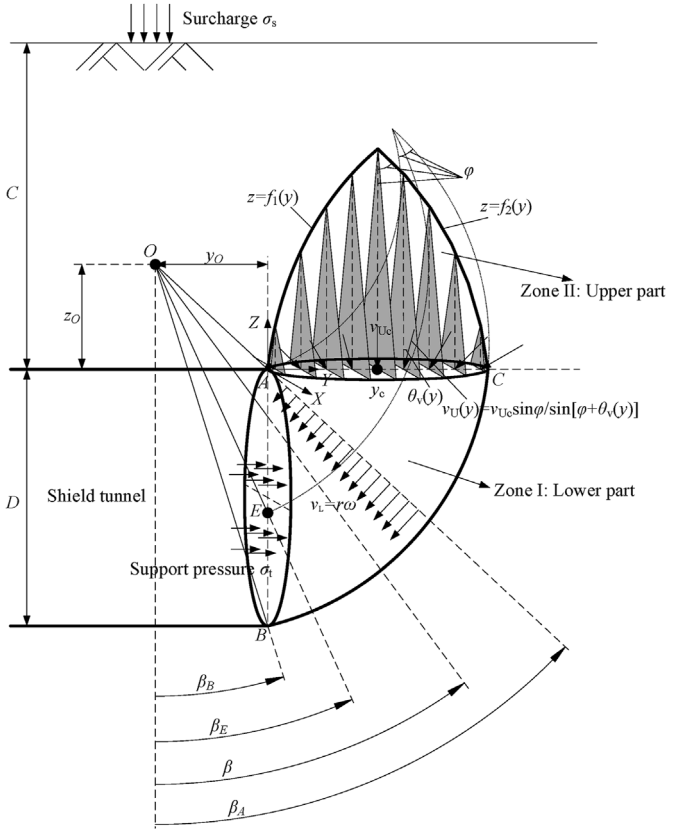

Fig. 12. Proposed 3D failure mechanism for a circular shield tunnel.

3.2.2. Principle of the point generation in Zone II

As shown in Fig. 18, all the points $P_{sj,1}$ discretize the contour of the intersection plane between Zones I and II. The determination on $P_{sj,1}$ is performed by testing all the facets $F_{i,j}$. When both $P'_{i,j}$ and $P_{i,j+1}$ are beyond the tunnel vault, then the point $P_{i,j+1}$ will be deleted. When both $P'_{i,j}$ and $P_{i,j+1}$ are below the tunnel vault, then the point $P_{i,j+1}$ will be preserved. But when $P'_{i,j}$ is below the tunnel vault while $P_{i,j+1}$ is beyond it, the intersection point between the line $P'_{i,j}P_{i,j+1}$ and the plane at the level of the tunnel vault will replace $P_{i,j+1}$ using a linear interpolation.

The obtained discretized points $P_{i,j}$ in the intersection plane between Zones I and II are all renamed as $P_{si,1}$, where $1 \le i \le n_s$ and n_s is the number of the obtained discretized points. The serial number i of the point $P_{si,1}$ is ranked counterclockwise as shown in Fig. 18. The angular parameter $\theta_{si,1}$ in the plane Π_{s1} is calculated as follows:

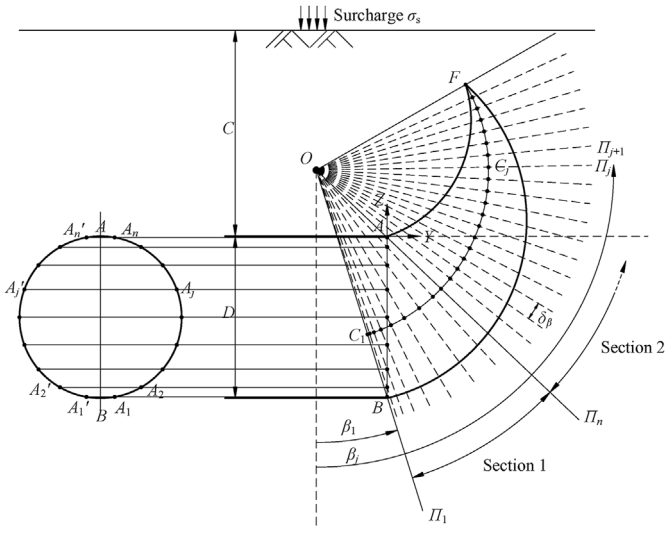

Fig. 13. Spatial discretization technique for the generation of the mechanism in Zone I.

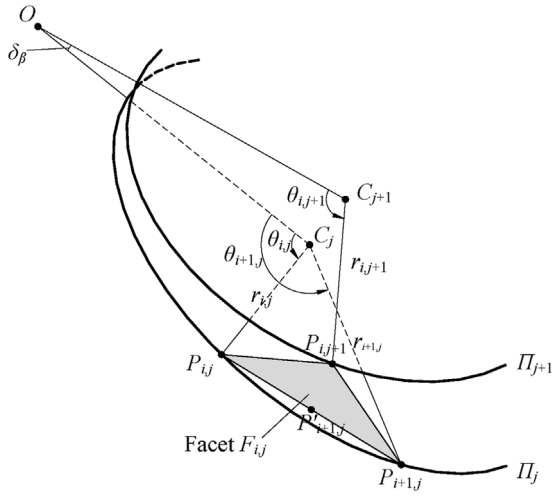

Fig. 14. Details of the point generation in Zone I.

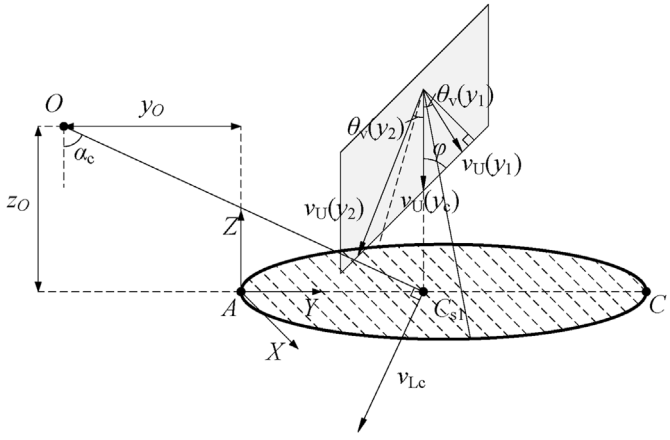

Fig. 15. Proposed velocity field in Zone II.

$$\theta_{si,1} = \arccos\left(\frac{\overrightarrow{C_{s1}P_{si,1}} \cdot \overrightarrow{C_{s1}A}}{\left|\overrightarrow{C_{s1}P_{si,1}}\right| \cdot \left|\overrightarrow{C_{s1}A}\right|}\right) \tag{14}$$

Each two points $P_{si,1}$ and $P_{si+1,1}$ of plane Π_{s1} can generate a new point $P_{si,2}$ of plane Π_{s2}. More generally, $P_{si,j}$ and $P_{si+1,j}$ of plane Π_{sj} can generate $P_{si,j+1}$ of plane Π_{sj+1}. Similarly, the point generation in Zone II should also respect the following three conditions:

(1) The angle between the normal vector $\vec{N}_{si,j}$ and the velocity vector of facet $F_{si,j}$ is equal to $\pi/2 + \varphi$.
(2) $P_{si,j+1}$ belongs to the plane Π_{sj+1}.
(3) The quasi-uniform distribution requires $\theta_{si,j+1} = (\theta_{si,j} + \theta_{si+1,j})/2$.

In the plane Π_{s1} (the intersection plane between Zones I and II. These n_s discretized points will generate n_s new points in the next plane Π_{s2}. This generation process will continue until the end of Zone II (the point C_{snh}).

3.2.3. Mathematical formulation for the point generation in Zone II

This section will illustrate the mathematical formulation for the point generation in detail, as shown in Fig. 19. $P_{si,j}$, $P_{si+1,j}$ and $P_{si,j+1}$ are given by

$$\left.\begin{aligned} P_{si,j} &= \left(x_{si,j}, y_{si,j}, z_{si,j}\right) \\ P_{si+1,j} &= \left(x_{si+1,j}, y_{si+1,j}, z_{si+1,j}\right) \\ P_{si,j+1} &= \left(x_{si,j+1}, y_{si,j+1}, z_{si,j+1}\right) \end{aligned}\right\} \tag{15}$$

Using Eq. (15), the vector $\overrightarrow{P_{si,j}P_{si+1,j}}$ and the midpoint $P'_{si,j}$ between the points $P_{si,j}$ and $P_{si+1,j}$ are given by

$$\left.\begin{aligned} \overrightarrow{P_{si,j}P_{si+1,j}} &= (a_{xsi,j}, a_{ysi,j}, a_{zsi,j}) \\ P'_{si,j} &= \left(x'_{si,j}, y'_{si,j}, z'_{si,j}\right) \end{aligned}\right\} \tag{16a}$$

where

$$\left.\begin{aligned} a_{xsi,j} &= x_{si+1,j} - x_{si,j} \\ a_{ysi,j} &= y_{si+1,j} - y_{si,j} \\ a_{zsi,j} &= z_{si+1,j} - z_{si,j} \end{aligned}\right\} \tag{16b}$$

$$\left.\begin{aligned} x'_{si,j} &= (x_{si,j} + x_{si+1,j})/2 \\ y'_{si,j} &= (y_{si,j} + y_{si+1,j})/2 \\ z'_{si,j} &= (z_{si,j} + z_{si+1,j})/2 \end{aligned}\right\} \tag{16c}$$

Moreover, the normal vector to the facet $F_{si,j}$ and the velocity vector of the facet $F_{si,j}$ are defined as follows:

$$\left.\begin{aligned} \vec{N}_{si,j} &= \left(x_{nsi,j}, y_{nsi,j}, z_{nsi,j}\right) \\ \vec{v}_{si,j} &= \left(v_{xsi,j}, v_{ysi,j}, v_{zsi,j}\right) \end{aligned}\right\} \tag{17}$$

According to the velocity field in Zone II, the expressions of the unit velocity vector are as follows:

$$\left.\begin{aligned} v_{xsi,j} &= 0 \\ v_{ysi,j} &= \sin\left[\theta_v\left(y'_{si,j}\right)\right] \\ v_{zsi,j} &= -\cos\left[\theta_v\left(y'_{si,j}\right)\right] \end{aligned}\right\} \tag{18}$$

In order to obey the normality condition, the following conditions must be satisfied:

$$\left.\begin{aligned} \vec{N}_{si,j} \cdot \vec{v}_{si,j} &= \cos(\pi/2 + \varphi) \\ \vec{N}_{si,j} \cdot \overrightarrow{P_{si,j}P_{si+1,j}} &= 0 \\ \left|\vec{N}_{si,j}\right| &= 1 \end{aligned}\right\} \tag{19}$$

By substituting Eqs. (16)-(18) into Eq. (19), the following conditions are obtained:

$$\left.\begin{aligned} x_{nsi,j}v_{xsi,j} + y_{nsi,j}v_{ysi,j} + z_{nsi,j}v_{zsi,j} &= \cos(\pi/2 + \varphi) \\ x_{nsi,j}a_{xsi,j} + y_{nsi,j}a_{ysi,j} + z_{nsi,j}a_{zsi,j} &= 0 \\ x^2_{nsi,j} + y^2_{nsi,j} + z^2_{nsi,j} &= 1 \end{aligned}\right\} \tag{20}$$

By solving Eq. (20), the unit normal vector $\vec{N}_{si,j}$ is obtained as follows:

$$\left.\begin{aligned} z_{nsi,j} &= \left(-F_{si,j} \pm \sqrt{\Delta_{si,j}}\right) \Big/ (2E_{si,j}) \\ y_{nsi,j} &= A_{si,j}z_{nsi,j} + B_{si,j} \\ x_{nsi,j} &= C_{si,j}z_{nsi,j} + D_{si,j} \end{aligned}\right\} \tag{21}$$

where the negative or positive sign of $z_{nsi,j}$ is to ensure $\vec{N}_{si,j}$ pointing outside. This condition can be satisfied by $\vec{N}_{si,j} \cdot (\overrightarrow{P_{si,j}P_{si+1,j}} \times$

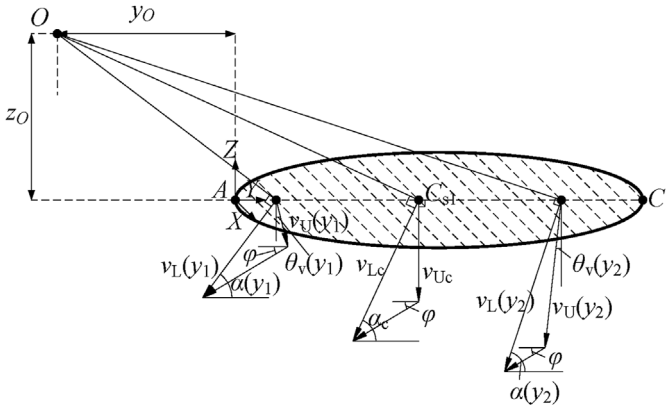

Fig. 16. Velocity relationship between Zones I and II.

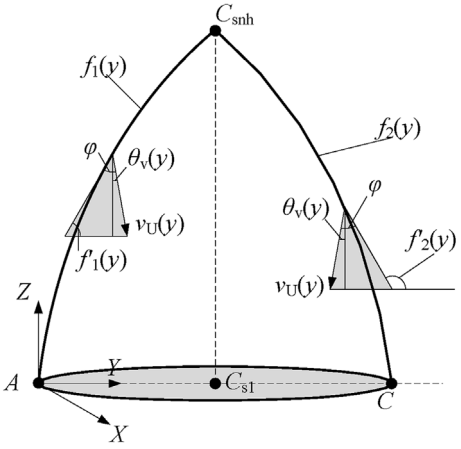

Fig. 17. Derivation of the failure mechanism in Zone II.

$\overrightarrow{v}_{si,j}) > 0$. The intermediate parameters in Eq. (21) are given as follows:

$$\left.\begin{aligned} A_{si,j} &= -v_{zsi,j}/v_{ysi,j} \\ B_{si,j} &= \cos(\pi/2+\varphi)/v_{ysi,j} \\ C_{si,j} &= (-A_{si,j}a_{ysi,j} - a_{zsi,j})/a_{zsi,j} \\ D_{si,j} &= -B_{si,j}a_{ysi,j}/a_{xsi,j} \\ E_{si,j} &= A_{si,j}^2 + C_{si,j}^2 + 1 \\ F_{si,j} &= 2A_{si,j}B_{si,j} + 2C_{si,j}D_{si,j} \\ G_{si,j} &= B_{si,j}^2 + D_{si,j}^2 - 1 \\ \Delta_{si,j} &= F_{si,j}^2 - 4E_{si,j}G_{si,j} \end{aligned}\right\} \tag{22}$$

The vector from the point C_{sj+1} to the point $P_{si,j+1}$ is given by

$$\overrightarrow{C_{sj+1}P_{si,j+1}} = r_{si,j+1}\,\overrightarrow{\delta}_{si,j+1} \tag{23}$$

where $r_{si,j+1}$ is the norm of the vector $\overrightarrow{C_{sj+1}P_{si,j+1}}$. The coordinates of the point C_{sj+1} are $(x_{Cs}, y_{Cs}, (z_{Cs}/n_h)j)$. $\overrightarrow{\delta}_{si,j+1}$ is the unit vector from the point C_{sj+1} to the point $P_{si,j+1}$ and can be expressed as follows:

$$\left.\begin{aligned} \delta_{xsi,j+1} &= \sin(\theta_{si,j+1}) \\ \delta_{ysi,j+1} &= -\cos(\theta_{si,j+1}) \\ \delta_{zsi,j+1} &= 0 \end{aligned}\right\} \tag{24}$$

The vector $\overrightarrow{P'_{si,j}P_{si,j+1}}$ in the facet $F_{si,j}$ must satisfy the following condition:

$$\begin{aligned} \overrightarrow{P'_{si,j}P_{si,j+1}} \cdot \overrightarrow{N}_{si,j} &= \left(\overrightarrow{P'_{si,j}C_{sj+1}} + \overrightarrow{C_{sj+1}P_{si,j+1}}\right) \cdot \overrightarrow{N}_{si,j} \\ &= \left(\overrightarrow{P'_{si,j}C_{sj+1}} + r_{si,j+1}\,\overrightarrow{\delta}_{si,j+1}\right) \cdot \overrightarrow{N}_{si,j} = 0 \end{aligned} \tag{25}$$

By substituting Eq. (24) into Eq. (25), $r_{si,j+1}$ is expressed as follows:

$$r_{si,j+1} = -\frac{x_{nsi,j}(x_{C_s} - x'_{si,j}) + y_{nsi,j}\left(y_{C_s} - y'_{si,j}\right) + z_{nsi,j}(\delta_h j - z'_{si,j})}{x_{nsi,j}\delta_{xsi,j+1} + y_{nsi,j}\delta_{ysi,j+1} + z_{nsi,j}\delta_{zsi,j+1}} \tag{26}$$

Thus the coordinates of the point $P_{si,j+1}$ is obtained:

$$\left.\begin{aligned} x_{si,j+1} &= x_{C_s} + r_{si,j+1}\delta_{xsi,j+1} \\ y_{si,j+1} &= y_{C_s} + r_{si,j+1}\delta_{ysi,j+1} \\ z_{si,j+1} &= \delta_h j + r_{si,j+1}\delta_{zsi,j+1} \end{aligned}\right\} \tag{27}$$

The point generation will successively proceed until the Z-coordinate of the newly generated point is greater than z_{Cs}. Besides, when the point C_{snh} is beyond the ground surface, the proposed mechanism outcrops. The intersection plane between the ground surface and Zone II needs to be determined. To determine this intersection plane, all the facets $F_{si,j}$ should be tested. When both $P'_{si,j}$ and $P_{si,j+1}$ are beyond the ground surface, $P_{si,j+1}$ will be deleted. When both $P'_{si,j}$ and $P_{si,j+1}$ are below the ground surface, $P_{si,j+1}$ will be preserved. When $P'_{si,j}$ is below the ground surface while $P_{si,j+1}$ is beyond it, the intersection point between the line $P'_{si,j}P_{si,j+1}$ and the ground surface will replace $P_{si,j+1}$ using a linear interpolation.

3.3. Work equation

The computation of the proposed model includes the calculations on the rate of the energy dissipation and the total work rates of all the external forces of the failure mechanism. To illustrate the procedure of the computation of the proposed model, a flowchart is provided in Fig. 20. First, the conditions of the soil property and the tunnel size should be given. Second, based on the associated flow rule, the failure mechanism of the tunnel face should be constructed to approximate the reality. Then, both the rate of the energy dissipation and the total work rates of all the external forces of the failure mechanism need to be calculated. Subsequently, the critical face pressure can be determined according to the limit analysis theorem. Thereafter, the obtained face pressure and failure pattern of the tunnel face should be verified by comparing with the existing studies, the numerical simulation, the model test and the field monitoring. At last, the constructed failure mechanism can be proven to be valid and reasonable if the obtained results are close to that of other studies.

According to Chen (1975), the following condition is required in the limit analysis method:

$$\dot{W}_D = \dot{W}_d + \dot{W}_s \geq \dot{W}_E = \dot{W}_{\sigma_t} + \dot{W}_{\sigma_s} + \dot{W}_\gamma \tag{28}$$

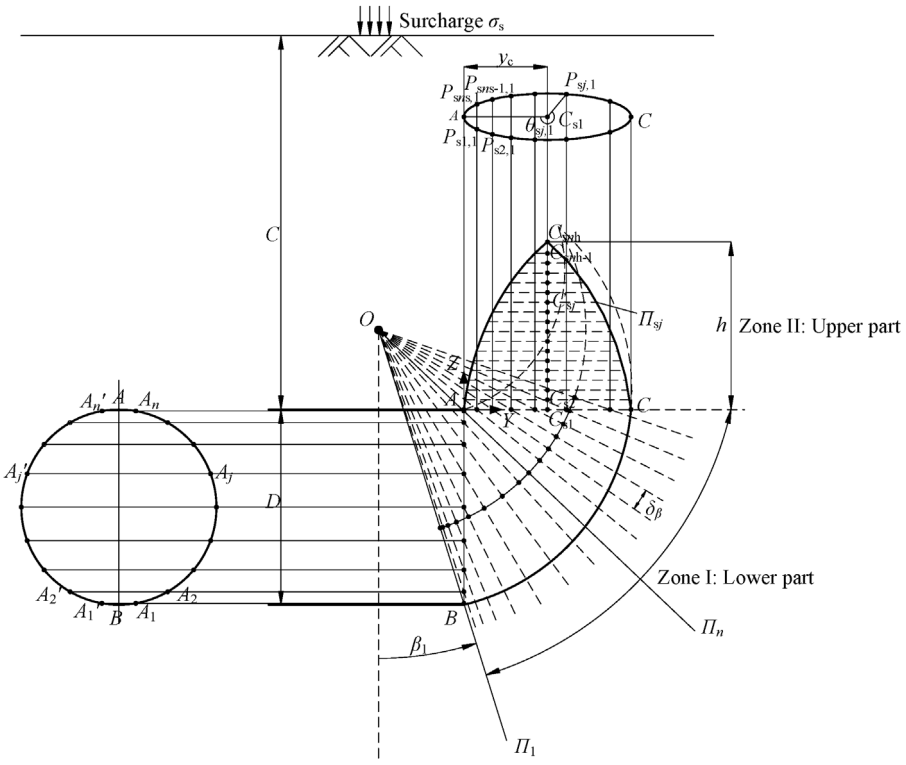

Fig. 18. Spatial discretization technique for the generation of the mechanism in Zone II.

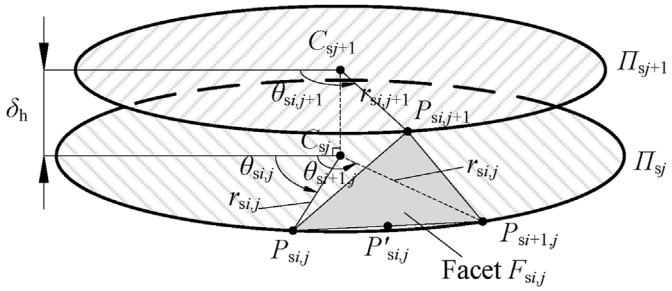

Fig. 19. Details of the point generation in Zone II.

where $\dot{W}_D$ represents the rate of energy dissipation; $\dot{W}_s$ and $\dot{W}_d$ are the rates of energy dissipation within the soil mass and along the failure surface, respectively; and $\dot{W}_E$ represents the total rate of work done by external forces, which includes the face pressure σ_t, the surcharge σ_s and the soil unit weight γ.

The rate of work is computed by the summation of the rate of work of each elementary area or volume. The calculation method of the elementary area and volume can be referred to Mollon et al. (2010, 2011).

The rate of work of the face pressure σ_t is calculated as follows:

$$\dot{W}_{\sigma_t} = \iint_{S_t} \left(\vec{\sigma}_t \cdot \vec{v} \right) \mathrm{d}S_t = \sum_j \left(\omega R_{tj} \sigma_t S_{tj} \cos \beta_{tj} \right) \tag{29}$$

where S_t is the tunnel face; S_{tj} is the elementary area of S_t; and R_{tj} and β_{tj} are the radius and angular parameters of the barycenter of the elementary facet S_{tj}, respectively.

The rate of work of the surcharge is calculated as follows:

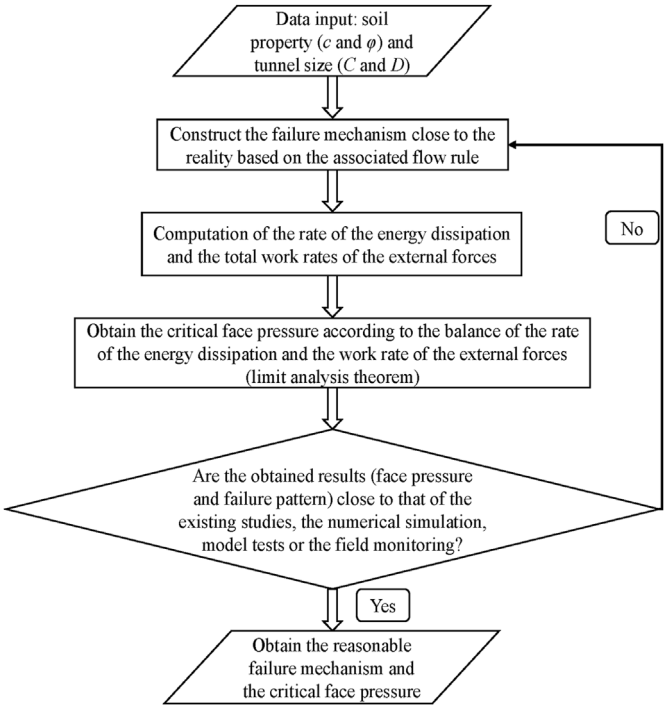

Fig. 20. Flowchart of the computation of the analytical model based on the limit analysis theorem.

$$\dot{W}_{\sigma_s} = \iint_{S_{su}} \left(\vec{\sigma}_s \cdot \vec{v} \right) \mathrm{d}S_{su} = \sum_j \left(v_{Uj} \sigma_s S_{suj} \cos \theta_{vj} \right) \tag{30}$$

where S_{su} is the intersection plane between Zone II and the ground surface, S_{suj} is the elementary area of S_{su}, and θ_{vj} is the angle

between the velocity v_{Uj} of S_{suj} and the negative direction of the Z-coordinate.

The rate of work of the soil weight includes two parts: $\dot{W}_{\gamma I}$ of Zone I and $\dot{W}_{\gamma II}$ of Zone II:

$$\left.\begin{aligned}\dot{W}_{\gamma I} &= \iiint_V (\vec{\gamma}\cdot\vec{v})\mathrm{d}V = \sum_j\sum_i\left(\omega\gamma R_{i,j}V_{i,j}\sin\beta_j\right)\\ \dot{W}_{\gamma_{II}} &= \iiint_{V_s} (\vec{\gamma}\cdot\vec{v})\mathrm{d}V_s = \sum_j\sum_i\left(v_{Ui,j}\gamma V_{si,j}\cos\theta_{vi,j}\right)\end{aligned}\right\} \tag{31}$$

where V and V_s are the volumes of Zones I and II, respectively; $V_{i,j}$ and $V_{si,j}$ are the corresponding elementary volumes of Zones I and II, respectively; $R_{i,j}$ and β_j represent the polar coordinates of $V_{i,j}$; $v_{Ui,j}$ is the velocity of the elementary block $V_{si,j}$; and $\theta_{vi,j}$ is the angle between the velocity $v_{Ui,j}$ and the negative direction of the Z-coordinate.

where S and S_s are the failure surfaces in Zones I and II, respectively; $S_{i,j}$ and $S_{si,j}$ are the corresponding elementary surfaces of S and S_s, respectively; $R_{i,j}$ represents the radial coordinate of the elementary surface $S_{i,j}$; $\dot{\varepsilon}_{max}$ is the maximal principal strain rate; $\dot{\varepsilon}_{maxi,j}$ is the maximal principal strain rate of the elementary block $V_{si,j}$; and v_{LUj} is the relative velocity on the elementary surface S_{IIIj} of the intersection plane S_{III} between Zones I and II. The formulae for the strain rate tensor are provided in Appendix A.

By substituting Eqs. (29)-(32) into Eq. (28) and equating the total rates of external force to the total rates of energy dissipation in Eq. (28), the critical face pressure can be obtained after some simplifications:

$$\sigma_t = \gamma D N_\gamma - cN_c + \sigma_s N_s \tag{33}$$

where N_γ, N_c and N_s represent the dimensionless parameters of soil unit weight γ, soil cohesion c and surcharge σ_s, respectively. N_γ, N_c and N_s are given as follows:

$$\left.\begin{aligned}N_\gamma &= \frac{\sum_j\sum_i\left(\omega R_{i,j}V_{i,j}\sin\beta_j\right)+\sum_j\sum_i\left(v_{Ui,j}V_{si,j}\cos\theta_{vi,j}\right)}{D\sum_j\left(\omega R_{tj}S_{tj}\cos\beta_{tj}\right)},\quad N_s = \frac{\sum_j\left(v_{Uj}S_{suj}\cos\theta_{vj}\right)}{\sum_j\left(\omega R_{tj}S_{tj}\cos\beta_{tj}\right)}\\ N_c &= \left\{\sum_j\sum_i\left(v_{Ui,j}\cos\varphi S_{si,j}\right)+\sum_j\sum_i\left[2\tan\left(\frac{\pi}{4}+\frac{\varphi}{2}\right)\dot{\varepsilon}_{maxi,j}V_{si,j}\right]+\sum_j\sum_i\left(\omega R_{i,j}\cos\varphi S_{i,j}\right)+\sum_j\left(v_{LUj}\cos\varphi S_{IIIj}\right)\right\}\Big/\sum_j\left(\omega R_{tj}S_{tj}\cos\beta_{tj}\right)\end{aligned}\right\} \tag{34}$$

The rate of energy dissipation also includes three parts: the rate of energy dissipation $\dot{W}_{DI}$ of Zone I, the rate of energy dissipation $\dot{W}_{DII}$ of Zone II, and $\dot{W}_{DIII}$ in the intersection plane between Zones I and II. In Zone I, a rotational velocity field is considered, thus only the soil plastic deformation $\dot{W}_{dI}$ along the failure surface leads to the energy dissipation. In Zone II, the proposed velocity field is continuous along the Y-coordinate, thus the energy dissipation includes $\dot{W}_{dII}$ occurring along the failure surface and $\dot{W}_{sII}$ undergoing within the soil mass. Besides, the energy dissipation along the velocity discontinuity plane between Zones I and II is represented by $\dot{W}_{dIII}$. The rate of energy dissipation is provided as follows:

$$\left.\begin{aligned}\dot{W}_{DI} &= \dot{W}_{dI} = \iint_S (cv\cos\varphi)\mathrm{d}S = \sum_j\sum_i\left(c\omega R_{i,j}\cos\varphi S_{i,j}\right)\\ \dot{W}_{DII} &= \begin{cases}\dot{W}_{dII} = \iint_{S_s}(cv\cos\varphi)\mathrm{d}S_s = \sum_j\sum_i\left(cv_{Ui,j}\cos\varphi S_{si,j}\right)\\ \dot{W}_{sII} = \iiint_{V_s}\left[2c\tan\left(\frac{\pi}{4}+\frac{\varphi}{2}\right)\dot{\varepsilon}_{max}\right]\mathrm{d}V_s = \sum_j\sum_i\left[2c\tan\left(\frac{\pi}{4}+\frac{\varphi}{2}\right)\dot{\varepsilon}_{maxi,j}V_{si,j}\right]\end{cases}\\ \dot{W}_{DIII} &= \dot{W}_{dIII} = \iint_{S_{III}}(cv\cos\varphi)\mathrm{d}S_{III} = \sum_j\left(cv_{LUj}\cos\varphi S_{IIIj}\right)\end{aligned}\right\} \tag{32}$$

The critical face pressure is determined by maximizing Eq. (33) with different coordinates (x_O, y_O). The constrained optimization procedure is performed with the software MATLAB. The discretization parameters are selected as follows: $n = 200$, $\delta_\beta = 0.1^\circ$ and $\delta_H = 0.01$ m, which are the compromises between accuracy and time-cost. The maximization formula is given as follows:

$$\max\sigma_t \quad \text{s.t.}\begin{cases}\alpha(y_A) > \varphi\\ \theta_v(y_A) \le \varphi\\ \theta_v(y_C) > \max\{\alpha(y_C) - \pi/2, -\varphi\}\end{cases} \tag{35}$$

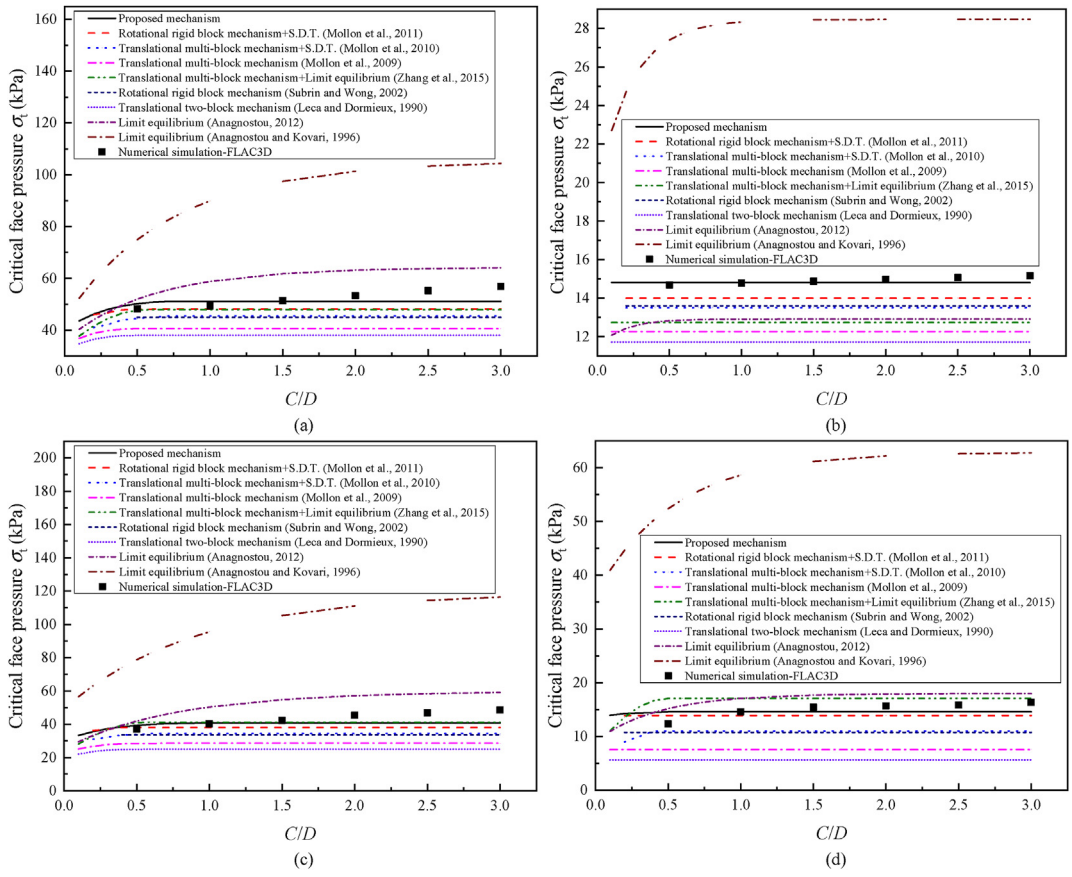

Fig. 21. Comparisons of the critical face pressure versus C/D for sands and clays: (a) $c = 0$ kPa and $\varphi = 20°$, (b) $c = 0$ kPa and $\varphi = 40°$, (c) $c = 7$ kPa and $\varphi = 17°$, and (d) $c = 10$ kPa and $\varphi = 25°$.

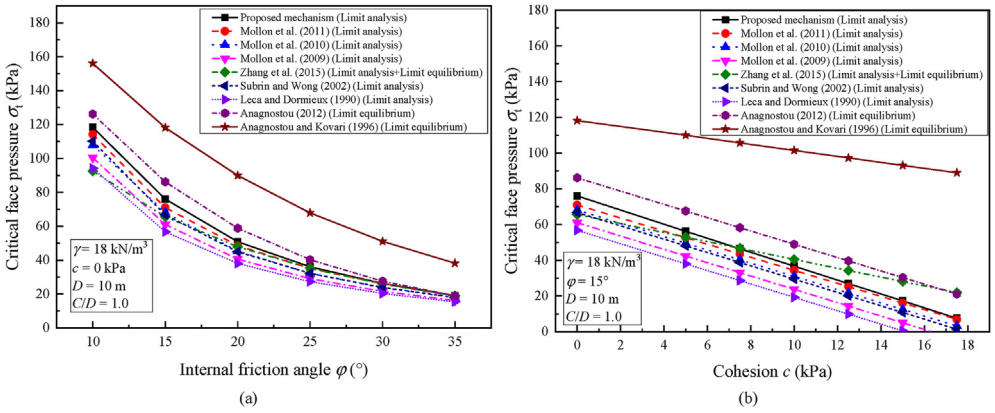

Fig. 22. Variations of the critical face pressure versus (a) internal friction angle φ and (b) cohesion c.

where these constrained conditions are set to ensure the normality condition in both Zones I and II.

4. Results and discussion

This section presents and discusses the results of the critical face pressure and failure pattern obtained from the proposed mechanism. To validate its accuracy, the proposed mechanism is compared with the numerical simulation and other studies. All the results are calculated based on the conditions of $D = 10$ m, $\gamma = 18$ kN/m^3 and $\sigma_s = 0$ kPa.

4.1. Comparison of the face pressure

Fig. 21a and b presents the comparisons of the critical face pressure for sands of $\varphi = 20°$ and 40°, respectively. It is shown that the critical face pressure increases with C/D when $C/D = 0$–1 and then remains constant when $C/D > 1$. This is because that the whole failure pattern is below the ground surface when $C/D > 1$, and the increase of the depth to diameter ratio will not influence the value of critical face pressure. In terms of the upper bound solutions, the proposed mechanism corresponds better with the numerical simulation and obviously improves the solutions obtained from the rotational and translational rigid block mechanisms adopting the

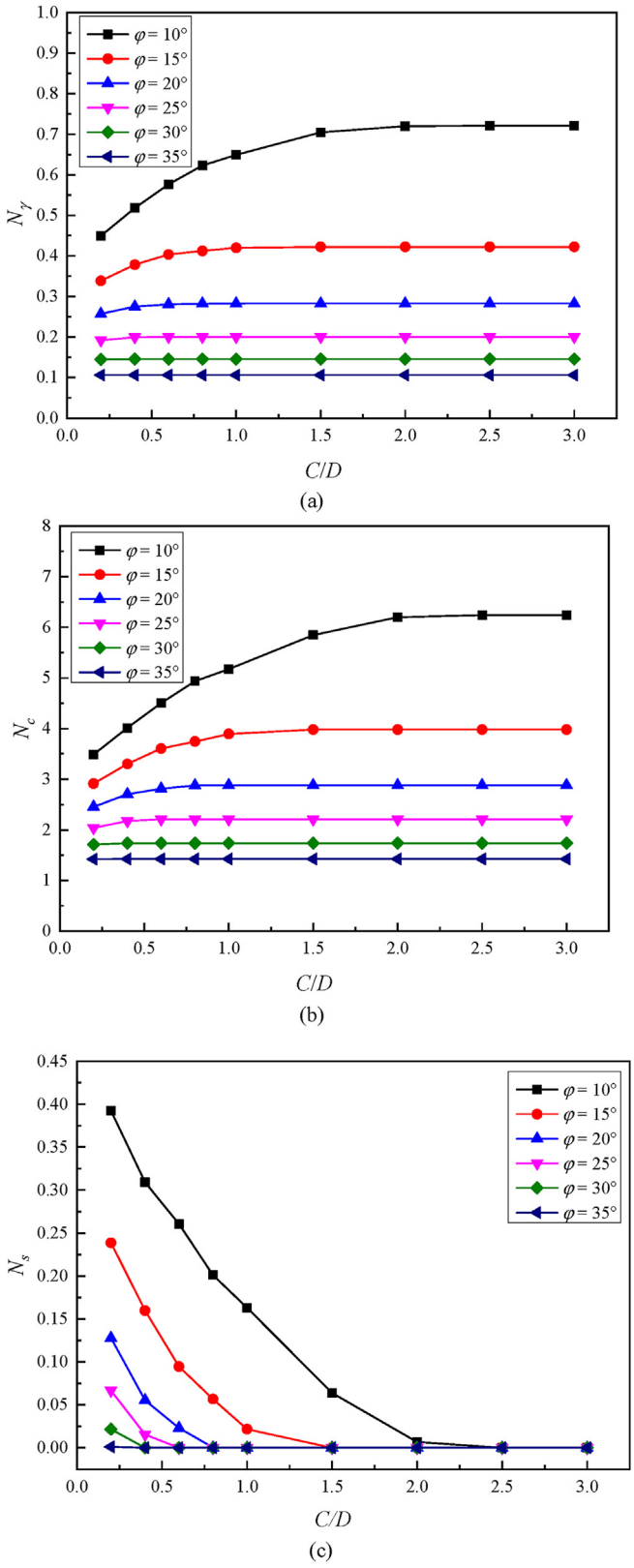

Fig. 23. Variations of the dimensionless parameters (a) N_γ, (b) N_c, and (c) N_s.

spatial discretization technique (S.D.T.) presented by Mollon et al. (2010, 2011). The improvements are 6.1% and 5.8% for $\varphi = 20°$ and 40° compared with Mollon et al. (2011), respectively.

Table 3
Dimensionless parameters N_γ, N_c and N_s.

C/D	Parameter	Internal friction angle φ (°)					
		10	15	20	25	30	35
0.2	N_γ	0.4495	0.3387	0.257	0.192	0.1449	0.1059
	N_c	3.4886	2.9121	2.4557	2.0391	1.7104	1.4238
	N_s	0.3924	0.2387	0.1279	0.0667	0.0217	0.0011
0.4	N_γ	0.5182	0.3783	0.2749	0.1997	0.1454	0.1059
	N_c	4.0127	3.3003	2.705	2.1751	1.7403	1.4253
	N_s	0.3091	0.1599	0.0553	0.0155	0	0
0.6	N_γ	0.5769	0.4036	0.2806	0.2005	0.1454	0.1059
	N_c	4.505	3.6044	2.8125	2.2108	1.7403	1.4253
	N_s	0.2607	0.0946	0.0229	0	0	0
0.8	N_γ	0.6229	0.4124	0.2824	0.2005	0.1454	0.1059
	N_c	4.9359	3.7448	2.8775	2.2108	1.7403	1.4253
	N_s	0.2012	0.0568	0.0003	0	0	0
1	N_γ	0.6494	0.42	0.2824	0.2005	0.1454	0.1059
	N_c	5.1722	3.8932	2.8799	2.2108	1.7403	1.4253
	N_s	0.1631	0.0217	0	0	0	0
1.5	N_γ	0.7046	0.4222	0.2824	0.2005	0.1454	0.1059
	N_c	5.8452	3.979	2.8799	2.2108	1.7403	1.4253
	N_s	0.064	0	0	0	0	0
2	N_γ	0.7203	0.4222	0.2824	0.2005	0.1454	0.1059
	N_c	6.1999	3.979	2.8799	2.2108	1.7403	1.4253
	N_s	0.0068	0	0	0	0	0
2.5	N_γ	0.7208	0.4222	0.2824	0.2005	0.1454	0.1059
	N_c	6.2384	3.979	2.8799	2.2108	1.7403	1.4253
	N_s	0	0	0	0	0	0
3	N_γ	0.7208	0.4222	0.2824	0.2005	0.1454	0.1059
	N_c	6.2384	3.979	2.8799	2.2108	1.7403	1.4253
	N_s	0	0	0	0	0	0

Compared with Mollon et al. (2010), the improvements can reach 12.4% and 9.7% for $\varphi = 20°$ and 40°, respectively. With respect to other kinematic approaches of the limit analysis (Leca and Dormieux, 1990; Subrin and Wong, 2002; Mollon et al., 2009), over 15% of the improvements are achieved. Besides, it is shown that the limit equilibrium methods generally provide a solution of greater value for the critical face pressure especially for Anagnostou and Kovári (1996) and Anagnostou (2012). Since the kinematic approach of the limit analysis and the limit equilibrium method are considered in two different ways, it is suggested that both methods should be taken into account to avoid over-conservative or critical estimate of the face stability.

Fig. 21c and d presents the comparisons of the critical face pressure for clays of $c = 7$ kPa, $\varphi = 17°$ and $c = 10$ kPa, $\varphi = 25°$, respectively. The results of the proposed mechanism are basically the same as that of the numerical simulation. The proposed mechanism improves the solutions obtained from Mollon et al. (2011) by 7.4% and 5.6% for $c = 7$ kPa, $\varphi = 17°$ and $c = 10$ kPa, $\varphi = 25°$, respectively. Compared with the results provided by Mollon et al. (2010), the improvements can attain 18.6% and 32.5% for $c = 7$ kPa, $\varphi = 17°$ and $c = 10$ kPa, $\varphi = 25°$, respectively. Moreover, it is shown that the solutions provided by the limit equilibrium method (Anagnostou and Kovári, 1996; Anagnostou, 2012; Zhang et al., 2015) generate larger values compared with the limit analysis (Leca and Dormieux, 1990; Mollon et al., 2009, 2010, 2011) in the case of sands. It is implied that the influence of cohesion is more pronounced in the kinematic approach of the limit analysis.

Fig. 22a and b presents the variations of the critical face pressure versus the internal friction angle φ and cohesion c, respectively. On the one hand, it can be seen that a nonlinear decreasing function between the critical face pressure σ_t and φ is observed. The improvement of the proposed mechanism with respect to the other kinematic mechanisms decreases with φ. This is because that the proposed mechanism improves the existing studies by providing a

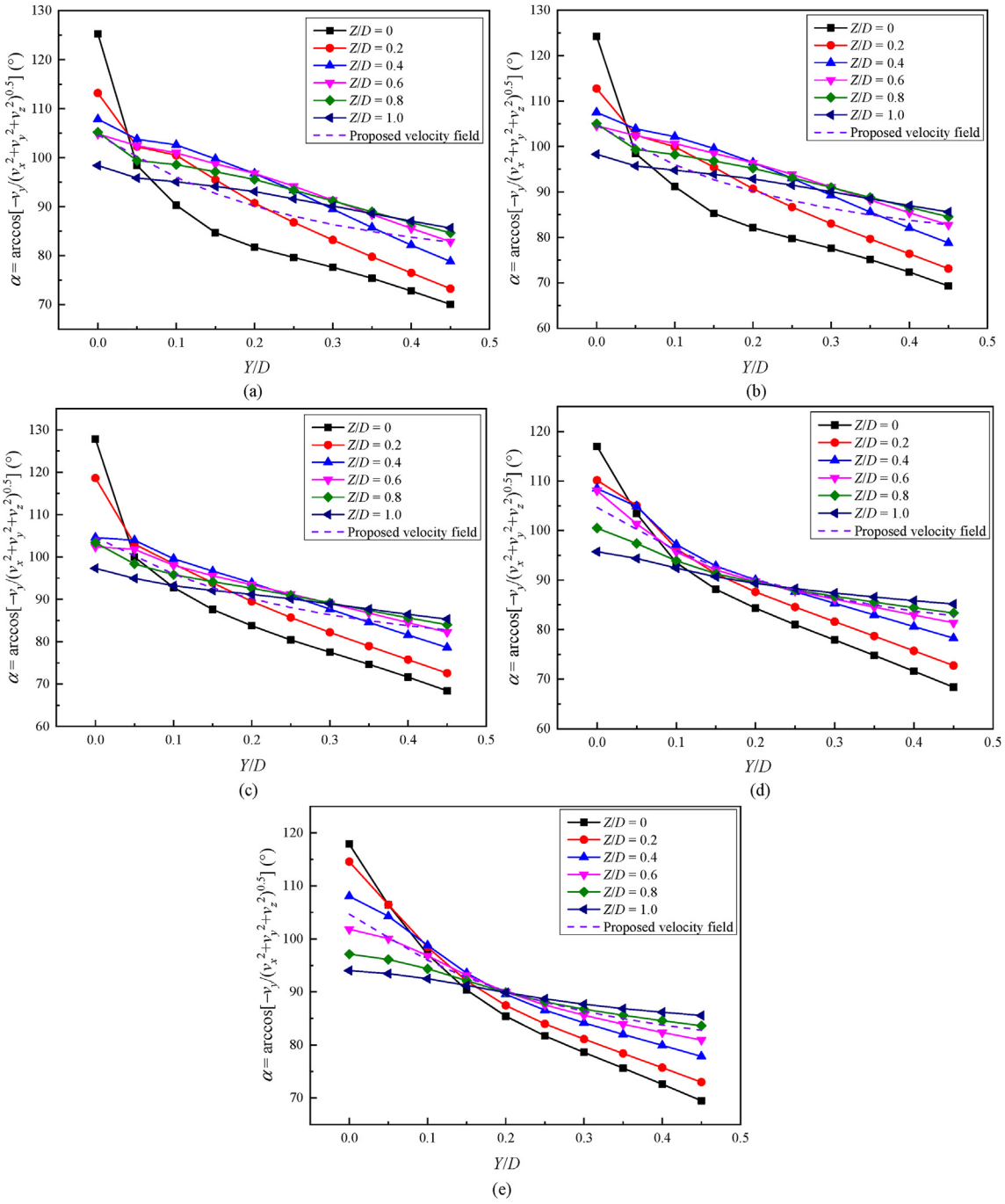

Fig. 24. Comparisons of the velocity inclination above tunnel vault in *Y-Z* cross-section: (a) $X/D = 0$, (b) $X/D = 0.08$, (c) $X/D = 0.24$, (d) $X/D = 0.39$, and (e) $X/D = 0.55$.

new velocity field above the tunnel vault. But the region of the failure mechanism above the tunnel vault decreases with φ, and thus the improvement decreases accordingly. On the other hand, the critical face pressure σ_t follows a linear function relationship of c. But the slopes of the lines provided by the limit equilibrium method are different from those provided by the limit analysis. It is suggested that the cohesion c has different effects on the face pressure in different methods. Compared with the limit analysis method, the influence of the cohesion c is reduced in the limit equilibrium method (Anagnostou and Kovári, 1996; Anagnostou, 2012; Zhang et al., 2015).

4.2. Design chart for the critical face pressure

According to Eq. (33), the critical face pressure can be calculated based on three dimensionless parameters N_γ, N_c and N_s. These parameters are almost independent of cohesion c but dependent on internal friction angle φ and relative depth ratio C/D. Fig. 23 provides the variations of N_γ, N_c and N_s versus C/D with different φ values. It is shown that both N_γ and N_c increase with C/D but decrease with φ. N_γ and N_c will remain constant when $C/D > 1$. Moreover, N_s decreases with both C/D and φ. The coefficient N_s represents the influence of the surcharge σ_s on the tunnel face, thus

N_s certainly becomes zero when the whole failure mechanism is below the ground surface and when C/D reaches a certain value.

Considering the use in the practical tunneling engineering, N_γ, N_c and N_s are provided in Table 3. This table can provide a quick calculation on the critical face pressure for different C/D and φ values.

4.3. Comparison of the velocity distribution

To validate the credibility of the proposed velocity field above the tunnel vault, the comparison of the velocity inclination above the tunnel vault in *Y-Z* cross-section obtained from the numerical simulation and the proposed velocity field for $c = 0$ kPa and $\varphi = 20°$ is shown in Fig. 24. The proposed failure mechanism above the tunnel vault extends to approximately 0.7*D* height above the tunnel vault (*Z*-direction), 0.4*D* ahead of tunnel face (*Y*-direction) and 0.5*D* in the horizontal direction (*X*-direction). Five vertical cross-sections ($X/D = 0–0.55$) with a range of $Z/D = 0–1$ and $Y/D = 0–0.45$ are selected to calculate the velocity inclination in the numerical simulation. It is shown that the velocity inclination of the proposed velocity field is basically consistent with that of the numerical simulation. The curve of the proposed velocity field is approximately the average value of the velocity inclination of $Z/D = 0–1$. The proposed velocity field can be considered as a reasonable hypothetical velocity field for the region above the tunnel vault in terms of the theoretical analysis.

Furthermore, the velocity vectors at the level of the tunnel vault provided by the proposed velocity field, the numerical simulation, the existing rotational and translational velocity fields are compared in Fig. 25. It is shown that the distributions of the existing rotational and translational velocity fields are totally different from that of the numerical simulation, while the proposed velocity field corresponds well to that of the numerical simulation. But it needs to be pointed out that the proposed velocity field provides a greater velocity magnitude on the far end at the level of the tunnel vault compared with the numerical simulation. It is caused by the requirement of the velocity compatibility between Zones I and II, and the velocity is assumed to keep constant in the vertical direction. Consequently, the proposed velocity field assumes a more severe situation of soil movement above the tunnel vault, which will provide a more conservative estimate of the face stability.

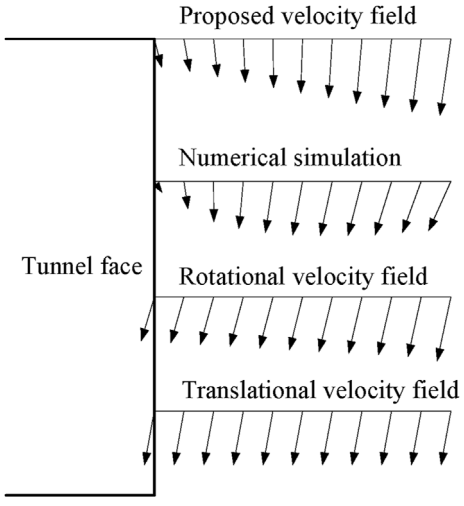

Fig. 25. Comparison of the velocity vector at the tunnel vault.

4.4. Comparison of the failure mechanism

Fig. 26a and b presents the 3D failure mechanism for sands and clays, respectively. Three perspectives are presented to show the failure pattern. The failure mechanism in sands of $c = 0$ kPa and $\varphi = 20°$ extends to about 0.7*D* height above the tunnel vault (*Z*-direction), 0.4*D* ahead of tunnel face (*Y*-direction) and approximately 0.5*D* in the horizontal direction (*X*-direction). With respect to the failure mechanism in clays of $c = 10$ kPa and $\varphi = 25°$, a stronger soil condition leads to a smaller failure region. The failure region is about 0.5*D* height above the tunnel vault, 0.4*D* ahead of tunnel face and approximately 0.5*D* in the horizontal direction for clays of $c = 10$ kPa and $\varphi = 25°$. The proposed failure mechanism presents a curved arch shape above the tunnel vault rather than a cone or horn shape in the existing rotational and translational rigid block mechanism. Besides, it is clear that the presented failure mechanisms are similar to the 3D images of the failure zone, as shown in Fig. 1.

Fig. 27 shows the comparisons among the proposed failure mechanism, the displacement contours of the numerical simulation and the exiting rotational and translational failure mechanisms. Zhang et al. (2015) defined the failure boundary according to the displacement contour. Based on this criterion, the proposed failure mechanism and the existing rotational and translational failure mechanisms all correspond well to the numerical simulation for the region ahead of the tunnel face. However, for the region above the tunnel vault, the shape, position and height of the soil arching of the rotational and translational failure mechanisms are different from the displacement contour. It is clear that the soil

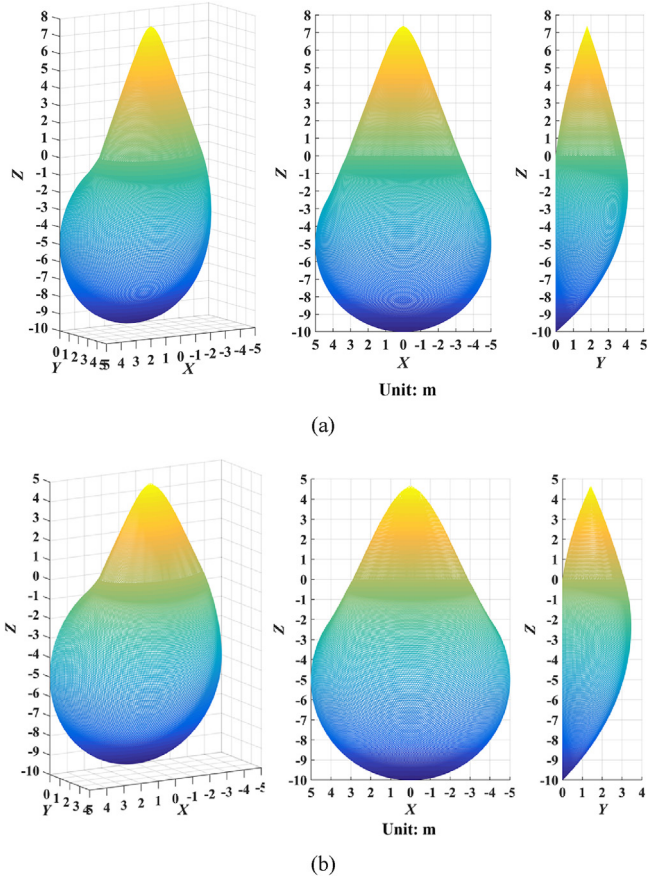

Fig. 26. Layout of the proposed failure mechanism for sands and clays: (a) $c = 0$ kPa, $\varphi = 20°$; and (b) $c = 10$ kPa, $\varphi = 25°$.

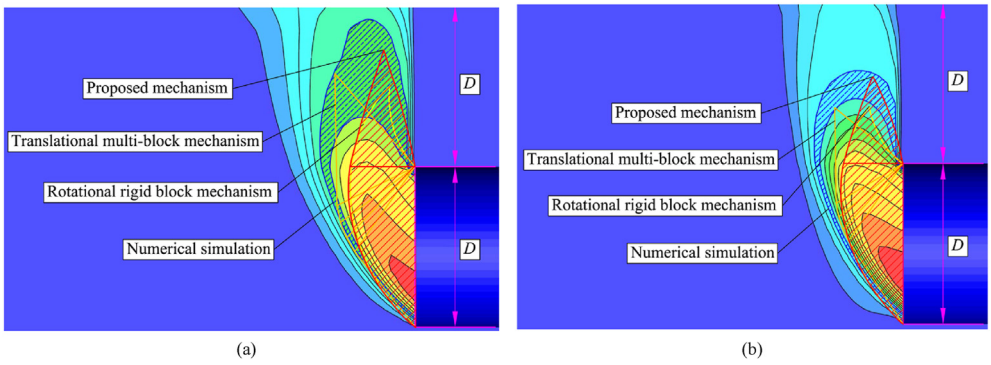

Fig. 27. Comparisons of the failure pattern: (a) $c = 0$ kPa, $\varphi = 20°$; and (b) $c = 10$ kPa, $\varphi = 25°$.

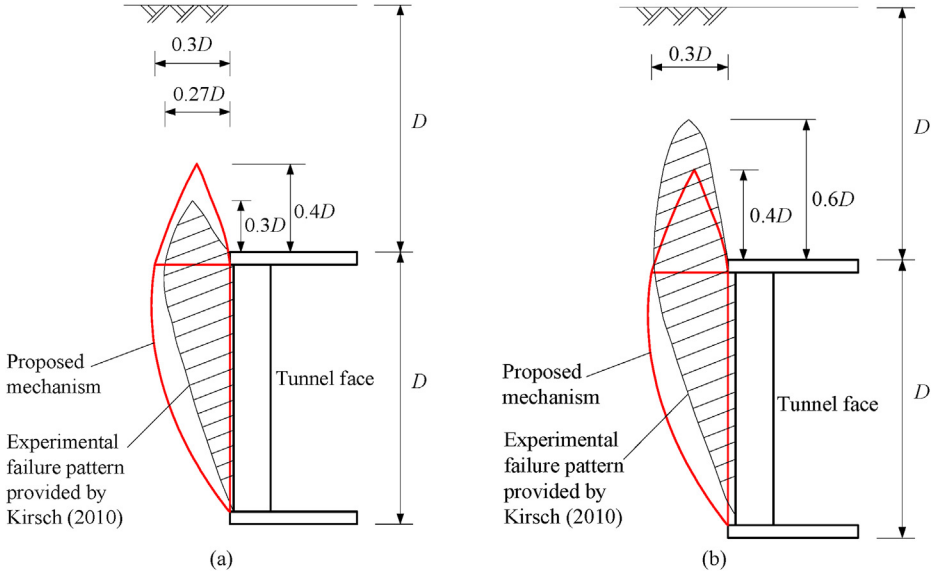

Fig. 28. Comparisons between the proposed mechanism and the incremental displacements.

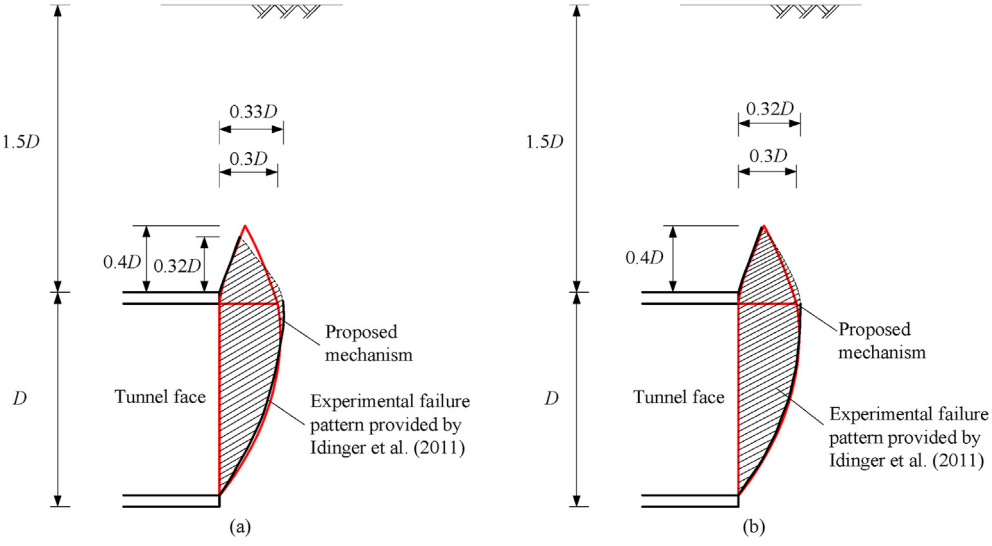

Fig. 29. Comparisons between the proposed mechanism and the contours of shear strain.

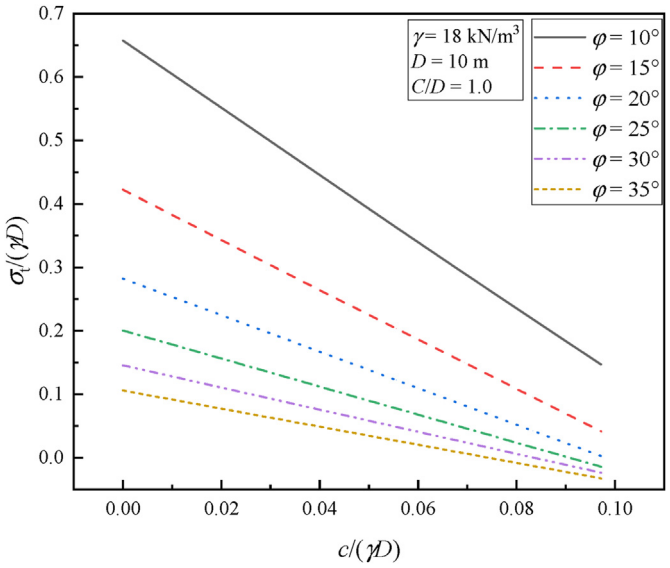

Fig. 30. Influence of the parameters of the Mohr-Coulomb yield criterion on the critical face pressure of the tunnel face.

arching of the proposed failure mechanism closely resembles that of the numerical simulation.

Fig. 28 shows the comparisons between the proposed mechanism and the incremental displacements obtained from the experimental test by Kirsch (2010). The incremental displacements can present both the moving soil body and the undisturbed soil region. The failure pattern of the tunnel face is thus easily determined from the visualization of the incremental displacement fields. It is well known that the failure pattern in the experimental test is closely related to the moment when the experimenter captures the failed soils. In this study, two cases of the failure patterns in the experimental test are compared with the proposed mechanism. Fig. 28a shows the incremental displacement for the piston simulating the tunnel face that advances from 1 mm to 1.25 mm. In this case, the proposed mechanism fully describes the failure pattern provided by the experimental test, which extends to only 0.3*D* above the tunnel vault and 0.27*D* ahead of the tunnel face. But when the piston advances from 2.25 mm to 2.5 mm as shown in Fig. 28b, the failure pattern provided by the experimental test propagates to about 0.6*D* above the tunnel vault and 0.3*D* ahead of the tunnel face, which is comparable to the proposed mechanism with a range of 0.4*D* high and 0.3*D* wide. In general, the proposed

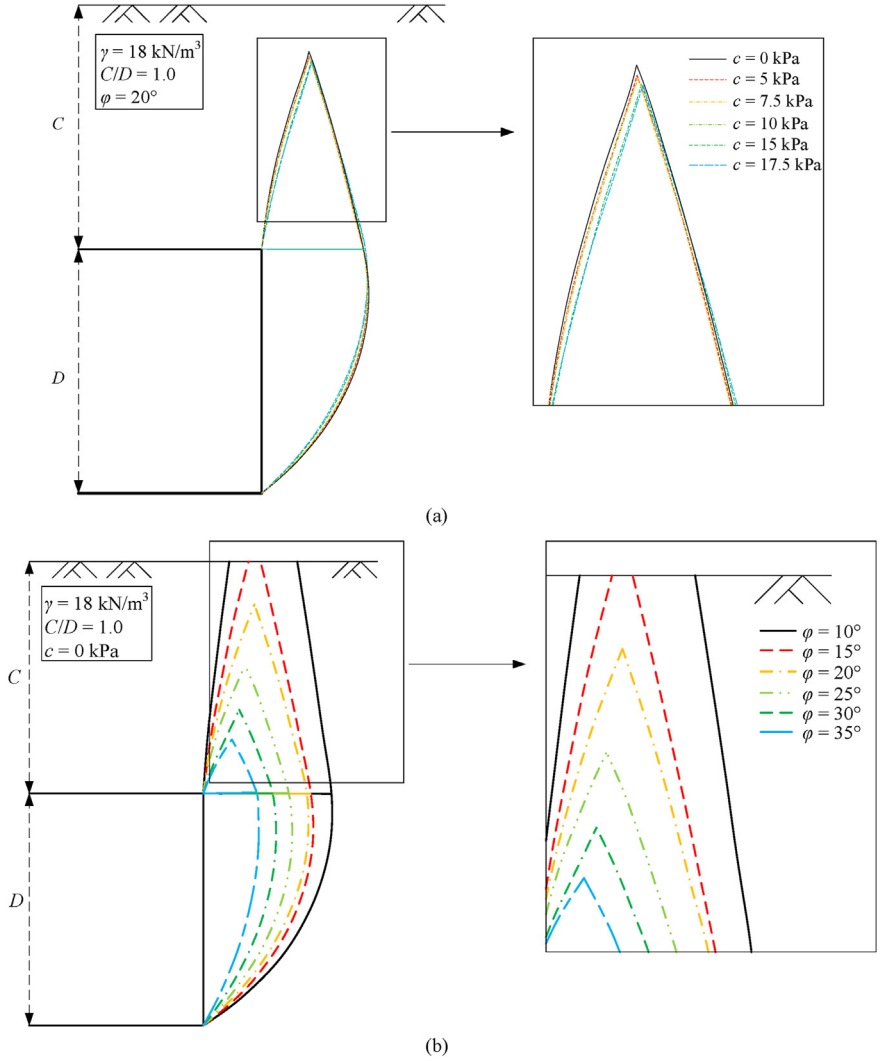

Fig. 31. Influences of the parameters of the Mohr-Coulomb yield criterion on the failure pattern of the tunnel face: (a) Influence of Cohesion, and (b) Influence of internal friction angle.

failure mechanism agrees well with the incremental displacement fields.

Fig. 29a and b presents the comparisons between the proposed mechanism and the contours of shear strain provided by the experimental test of Idinger et al. (2011) for piston displacements of 1.5 mm and 2.5 mm, respectively. The contours of shear strain can accurately describe the shear bands of soils. It is shown that the proposed mechanism complies with the shear bands of the experimental test in both cases. Both the proposed mechanism and the experimental failure pattern are approximately 0.3D ahead of the tunnel face and 0.4D above the tunnel vault. It is implied that the shear strain contour obtained from the experimental test is suitable for determining the boundary of the failed soils.

4.5. Influence of the Mohr-Coulomb parameters

Fig. 30 shows the influence of the parameters of the Mohr-Coulomb yield criterion on the critical face pressure of the tunnel. It is shown that the dimensionless critical face pressure decreases linearly with the dimensionless parameter of cohesion, and the variation gradient decreases with the internal friction angle. It is suggested that the cohesion of the Mohr-Coulomb yield criterion has a greater influence on the critical face pressure with a smaller internal friction angle. Fig. 30 also implies that the critical face pressure of the tunnel face can be easily obtained from the interpolation calculation according to the linear relationship between the critical face pressure and cohesion, which provides a convenient approach for the practicing engineers to estimate the stability of the tunnel face with the given conditions.

Fig. 31 shows the influence of the parameters of the Mohr-Coulomb yield criterion on the failure pattern of the tunnel face. Compared with the internal friction angle, the cohesion has a subtle influence on the failure pattern of the tunnel face as the failure zone decreases slightly with the cohesion. But the internal friction angle obviously affects both the range and position of the failure pattern of the tunnel face. With the decrease of the internal friction angle, the failure pattern of the tunnel face tends to expand in both the longitudinal and vertical directions. For the tunnel of $C/D = 1$ in the soils having $\gamma = 18$ kN/m^3 and $c = 0$ kPa, the collapse of the tunnel face will influence the ground surface when the internal friction angle decreases to 15°. Thus, it is considered that the internal friction angle of the Mohr-Coulomb yield criterion plays a more vital role in the performance of the proposed analytical model compared with the cohesion. Because the internal friction angle is closely related to the associated flow rule adopted in the limit analysis theorem, which inherently changes the failure pattern of the tunnel face and influences the upper solution of the critical face pressure.

5. Conclusions

Both numerical simulation and theoretical analysis were carried out to assess the face stability in frictional soils. A series of numerical simulations for different C/D and soil conditions was performed to investigate the velocity distribution of the tunnel face. According to the quantitative results of the numerical simulations, a kinematically admissible velocity field for the soil arching zone was proposed to construct a new failure mechanism based on the spatial discretization technique. Both the critical face pressure and the failure pattern were compared with the results of the numerical simulations and the existing studies to verify its accuracy. The main conclusions are given as follows:

(1) The results of the numerical simulations showed that the existing rotational velocity field can reasonably simulate the soil movement at the tunnel face. But both the rotational and translational velocity fields could not represent the velocity distribution above the tunnel vault.
(2) The proposed mechanism obviously improved the critical face pressure estimation of the existing analytical studies. The critical face pressure provided by the proposed mechanism corresponded well to that of the numerical simulation.
(3) The proposed mechanism presented a curved arch shape for the soil arching zone rather than a cone or 'horn' shape in the existing analytical methods. The proposed mechanism adequately reflect the failure patterns obtained from the numerical simulation and the experimental tests.
(4) The dimensionless parameters N_γ, N_c and N_s for different φ and C/D values were provided to calculate the critical face pressure. N_γ, N_c and N_s all decreased with φ. C/D would only impact N_γ, N_c and N_s when the failure mechanism outcropped at the ground surface.

Declaration of competing interest

The authors declare that they have no known competing financial interests or personal relationships that could have appeared to influence the work reported in this paper.

Acknowledgments

The authors acknowledge the financial support provided by the National Natural Science Foundation of China (Grant No. 51978042).

Appendix A. Supplementary data

Supplementary data to this article can be found online at https://doi.org/10.1016/j.jrmge.2021.10.006.

References

Anagnostou, G., 2012. The contribution of horizontal arching to tunnel face stability. Geotechnik 35, 34–44.
Anagnostou, G., Kovári, K., 1996. Face Stability conditions with earth-pressure-balanced shields. Tunn. Undergr. Space Technol. 11, 165–173.
Augarde, C.E., Lyamin, A.V., Sloan, S.W., 2003. Prediction of undrained sinkhole collapse. J. Geotech. Geoenviron. Eng. 129, 197–205.
Atkinson, J.H., Potts, D.M., 1977. Stability of a shallow circular tunnel in cohesionless soil. Geotechnique 27, 203–215.
Anagnostou, G., Perazzelli, P., 2013. The stability of a tunnel face with a free span and a non-uniform support. Geotechnik 36, 40–50.
Anagnostou, G., Perazzelli, P., 2015. Analysis method and design charts for bolt reinforcement of the tunnel face in cohesive-frictional soils. Tunn. Undergr. Space Technol. 47, 162–181.
Broms, B., Bennermark, H., 1967. Stability of Clay at vertical opening. J. Soil Mech. Found Div. 193, 71–94.
Chen, W.F., 1975. Limit Analysis and Soil Plasticity. Elsevier, Amersterdam, the Netherlands.
Chambon, P., Corte, J.F., 1994. Shallow tunnels in cohesionless soil: stability of tunnel face. J. Geotech Eng 120, 1148–1165.
Chen, R.P., Li, J., Kong, L.G., Tang, L.J., 2013. Experimental study on face instability of shield tunnel in sand. Tunn. Undergr. Space Technol. 33, 12–21.
Chen, R.P., Tang, L.J., Ling, D.S., Chen, Y.M., 2011. Face stability analysis of shallow shield tunnels in dry sandy ground using the discrete element method. Comput. Geotech. 38, 187–195.
De Buhan, P., Cuvillier, A., Dormieux, L., Maghous, S., 1999. Face stability of shallow circular tunnels driven under the water table: a numerical analysis. Int. J. Numer. Anal. Methods GeoMech. 23, 79–95.
Du, D., Dias, D., Do, N., 2020. Effect of surcharge loading on horseshoe-shaped tunnels excavated in saturated soft rocks. J. Rock Mech. Geotech. Eng. 12, 1339–1346.
Davis, E.H., Gunn, M.J., Mair, R.J., Seneviratne, H.N., 1980. The stability of shallow tunnels and underground openings in cohesive material. Geotechnique 30, 397–416.
Ding, W.T., Li, S.C., Liu, K.Q., Zhu, J., Li, M.J., Shi, P.H., 2018. Using a pressurized shield to increase face stability of circular tunnels in purely cohesive soil. Int. J. GeoMech. 18, 04018100.

Ding, W.T., Liu, K.Q., Shi, P.H., Li, M.J., Hou, M.L., 2019. Face stability analysis of shallow circular tunnels driven by a pressurized shield in purely cohesive soils under undrained conditions. Comput. Geotech. 107, 110–127.
Huang, M.S., Li, S., Yu, J., Tan Qi Wen, J., 2018a. Continuous field based upper bound analysis for three-dimensional tunnel face stability in undrained clay. Comput. Geotech. 94, 207–213.
Huang, M.S., Tang, Z., Zhou, W.X., Yuan, J.Y., 2018b. Upper bound solutions for face stability of circular tunnels in non-homogeneous and anisotropic clays. Comput. Geotech. 98, 189–196.
Han, K.H., Zhang, C.P., Li, W., Guo, C.X., 2016a. Face stability analysis of shield tunnels in homogeneous soil overlaid by multilayered cohesive-frictional soils. Math. Probl Eng. 2016, 1378274.
Han, K.H., Zhang, C.P., Zhang, D.L., 2016b. Upper-bound solutions for the face stability of a shield tunnel in multilayered cohesive-frictional soils. Comput. Geotech. 79, 1–9.
Idinger, G., Aklik, P., Wu, W., Borja, R.I., 2011. Centrifuge model test on the face stability of shallow tunnel. Acta Geotech 6, 105–117.
Kirsch, A., 2010. Experimental investigation of the face stability of shallow tunnels in sand. Acta Geotech 5, 43–62.
Klar, A., Klein, B., 2014. Energy-based volume loss prediction for tunnel face advancement in clays. Geotechnique 64, 776–786.
Keawsawasvong, S., Ukritchon, B., 2019. Undrained stability of a spherical cavity in cohesive soils using finite element limit analysis. J. Rock Mech. Geotech. Eng. 11, 1274–1285.
Klar, A., Osman, A.S., Bolton, M., 2007. 2D and 3D upper bound solutions for tunnel excavation using "elastic" flow fields. Int. J. Numer. Anal. Methods GeoMech. 31, 1367–1374.
Li, P.F., Chen, K.Y., Wang, F., Li, Z., 2019a. An upper-bound analytical model of blow-out for a shallow tunnel in sand considering the partial failure within the face. Tunn. Undergr. Space Technol. 91, 102989.
Leca, E., Dormieux, L., 1990. Upper and lower bound solutions for the face stability of shallow circular tunnels in frictional material. Geotechnique 40, 581–606.
Li, P.F., Wang, F., Zhang, C.P., Li, Z., 2019b. Face stability analysis of a shallow tunnel in the saturated and multilayered soils in short-term condition. Comput. Geotech. 107, 25–35.
Li, W., Zhang, C.P., 2020. Face stability analysis for a shield tunnel in anisotropic sands. Int. J. GeoMech. 20, 04020043.
Li, W., Zhang, C.P., Zhang, X., 2018. Stability analysis of the tunnel face in the cohesive-frictional soils considering the arch effect and rotational mechanism. J. Chin. Inst. Eng. 41, 697–709.
Li, W., Zhang, C.P., Zhu, W.J., Zhang, D.L., 2019c. Upper-bound solutions for the face stability of a non-circular NATM tunnel in clays with a linearly increasing undrained shear strength with depth. Comput. Geotech. 114, 103136.
Mair, R.J., 1969. Centrifugal Modelling of Tunnel Construction in Soft Clay. PhD Thesis. University of Cambridge, England, UK.
Mollon, G., Dias, D., Soubra, A.H., 2009. Probabilistic analysis and design of circular tunnels against face stability. Int. J. GeoMech. 9, 237–249.
Mollon, G., Dias, D., Soubra, A.H., 2010. Face stability analysis of circular tunnels driven by a pressurized shield. J. Geotech. Geoenviron. Eng. 136, 215–229.
Mollon, G., Dias, D., Soubra, A.H., 2011. Rotational failure mechanisms for the face stability analysis of tunnels driven by a pressurized shield. Int. J. Numer. Anal. Methods GeoMech. 35, 1363–1388.
Mollon, G., Dias, D., Soubra, A.H., 2013. Continuous velocity fields for collapse and blowout of a pressurized tunnel face in purely cohesive soil. Int. J. Numer. Anal. Methods GeoMech. 35, 2061–2083.
Osman, A.S., Mair, R.J., Bolton, M.D., 2006. On the kinematics of 2D tunnel collapse in undrained clay. Geotechnique 56, 585–595.
Pan, Q.J., Dias, D., 2016a. Face stability analysis for a shield-driven tunnel in anisotropic and nonhomogeneous soils by the kinematical approach. Int. J. GeoMech. 16, 04015076.
Pan, Q.J., Dias, D., 2016b. The effect of pore water pressure on tunnel face stability. Int. J. Numer. Anal. Methods GeoMech. 40, 2123–2136.
Pan, Q.J., Dias, D., 2017. Upper-bound analysis on the face stability of a non-circular tunnel. Tunn. Undergr. Space Technol. 62, 96–102.
Perazzelli, P., Leone, T., Anagnostou, G., 2014. Tunnel face stability under seepage flow conditions. Tunn. Undergr. Space Technol. 43, 459–469.
Schofield, A.N., 1980. Cambridge geotechnical centrifuge operations. Geotechnique 30, 227–268.
Shiau, J., Al-Asadi, F., 2020. Determination of critical tunnel heading pressures using stability factors. Comput. Geotech. 119, 103345.
Subrin, D., Wong, H., 2002. Tunnel face stability in frictional material: a new 3D failure mechanism. Compt. Rendus Mec. 330, 513–519.
Takano, D., Otani, J., Nagatani, H., Mukunoki, T., 2006. Application of X-ray CT on boundary value problems in geotechnical engineering - research on tunnel face failure. In: GeoCongress 2006. American Society of Civil Engineers (ASCE), pp. 1–6.
Ukritchon, B., Keawsawasvong, S., 2017. Design equations for undrained stability of opening in underground walls. Tunn. Undergr. Space Technol. 214–220.
Ukritchon, B., Keawsawasvong, S., Yingchaloenkitkhajorn, K., 2017a. Undrained face stability of tunnels in Bangkok subsoils. Int. J. Geotech. Eng. 11, 262–277.
Ukritchon, B., Yingchaloenkitkhajorn, K., Keawsawasvong, S., 2017b. Three-dimensional undrained tunnel face stability in clay with a linearly increasing shear strength with depth. Comput. Geotech. 88, 146–151.
Ukritchon, B., Keawsawasvong, S., 2019a. Stability of unlined square tunnels in Hoek-Brown rock masses based on lower bound analysis. Comput. Geotech. 105, 249–264.
Ukritchon, B., Keawsawasvong, S., 2019b. Lower bound stability analysis of plane strain headings in Hoek-Brown rock masses. Tunn. Undergr. Space Technol. 84, 99–112.
Ukritchon, B., Keawsawasvong, S., 2019c. Stability of retained soils behind underground walls with an opening using lower bound limit analysis and second-order cone programming. Geotech. Geol. Eng. 37, 1609–1625.
Vermeer, P.A., Ruse, N., Marcher, T., 2002. Tunnel heading stability in drained ground. Felsbau 20, 8–18.
Zou, J.F., Chen, G.H., Qian, Z.H., 2019a. Tunnel face stability in cohesion-frictional soils considering the soil arching effect by improved failure models. Comput. Geotech. 106, 1–17.
Zhang, C.P., Han, K.H., Zhang, D.L., 2015. Face stability analysis of shallow circular tunnels in cohesive-frictional soils. Tunn. Undergr. Space Technol. 50, 345–357.
Zhang, F., Gao, Y.F., Wu, Y.X., Zhang, N., 2018a. Upper-bound solutions for face stability of circular tunnels in undrained clays. Geotechnique 68, 76–85.
Zhang, F., Gao, Y.F., Wu, Y.X., Wang, Z.X., 2018b. Face stability analysis of large-diameter slurry shield-driven tunnels with linearly increasing undrained strength. Tunn. Undergr. Space Technol. 78, 178–187.
Zhang, C.P., Li, W., Zhu, W.J., Tan, Z.B., 2020. Face stability analysis of a shallow horseshoe-shaped shield tunnel in clay with a linearly increasing shear strength with depth. Tunn. Undergr. Space Technol. 97, 103291.
Zou, J.F., Qian, Z.H., 2018. Face-stability analysis of tunnels excavated below groundwater considering coupled flow deformation. Int. J. GeoMech. 18, 04018089.
Zou, J.F., Qian, Z.H., Xiang, X.H., Chen, G.H., 2019b. Face stability of a tunnel excavated in saturated nonhomogeneous soils. Tunn. Undergr. Space Technol. 83, 1–17.

Chengping Zhang obtained his BSc, MSc and PhD degrees in Civil Engineering from Beijing Jiaotong University. He was affiliated as the professor and head of the Department of Tunneling and Underground Engineering, School of Civil Engineering, Beijing Jiaotong University, and the member of the Bridge and Tunnel Committee and Standardization (tunnel) Professional Technical Committee of China Railway Society. He has been long engaged in the researches on the safety evaluation and control of the tunnel and underground engineering. He has led a number of research projects including the National Natural Science Foundation of China (NSFC), National Science and Technology Support Program and several researches on the highway tunnel, railway tunnel and subway tunnel for the enterprises.